

Bassoon proteinopathy drives neurodegeneration in multiple sclerosis

Benjamin Schattling^{1,9}, Jan Broder Engler^{1,9}, Constantin Volkmann¹, Nicola Rothhammer¹, Marcel S. Woo¹, Meike Petersen², Iris Winkler¹, Max Kaufmann¹, Sina C. Rosenkranz¹, Anna Fejtova^{3,4}, Ulrich Thomas³, Aparajita Bose¹, Simone Bauer¹, Simone Träger¹, Katharine K. Miller², Wolfgang Brück⁵, Kent E. Duncan², Gabriela Salinas⁶, Peter Soba², Eckart D. Gundelfinger^{3,7}, Doron Merkler⁸ and Manuel A. Friese^{1*}

Multiple sclerosis (MS) is characterized by inflammatory insults that drive neuroaxonal injury. However, knowledge about neuron-intrinsic responses to inflammation is limited. By leveraging neuron-specific messenger RNA profiling, we found that neuroinflammation leads to induction and toxic accumulation of the synaptic protein bassoon (Bsn) in the neuronal somata of mice and patients with MS. Neuronal overexpression of Bsn in flies resulted in reduction of lifespan, while genetic disruption of Bsn protected mice from inflammation-induced neuroaxonal injury. Notably, pharmacological proteasome activation boosted the clearance of accumulated Bsn and enhanced neuronal survival. Our study demonstrates that neuroinflammation initiates toxic protein accumulation in neuronal somata and advocates proteasome activation as a potential remedy.

Multiple sclerosis (MS) is the predominant cause of neurological impairment during early adulthood in northern latitudes. The disease has a massive impact on patients' quality of life and causes a substantial socioeconomic burden. It is estimated that 2.3 million people are living with MS globally, although this is probably an underestimation due to lack of precise data. The pathogenesis of the disease has been attributed to a breakdown of immune tolerance toward CNS antigens, which leads to inflammatory infiltrates that foster neuroaxonal injury¹. Neuroaxonal loss occurs early on in the course of the disease and is decisive for clinical deficits in patients². While great progress has been made in understanding and controlling the inflammatory component of the disease, the pathophysiological mechanisms of neuroaxonal injury are still not understood and only poorly affected by immunomodulatory drugs. Therefore, halting neurodegeneration in MS is a major unmet clinical need. Understanding the molecular pathways of inflammation-induced neurodegeneration holds the promise to translate this knowledge into a genuine neuroprotective treatment that slows disability progression and ensures continued socioeconomic participation of affected individuals.

The first insights into the pathological mechanisms of inflammation-induced neuroaxonal injury have been obtained in studies focusing on oxidative stress, mitochondrial dysfunction and ion channel activity². Chronic inflammation in MS results in the production of reactive oxygen and nitrogen species that probably promote neuronal mitochondrial injury as a result of detrimental mitochondrial DNA mutations that compromise mitochondrial function³. Inflammation also triggers the collapse of the mitochondrial

transmembrane potential and cessation of oxidative phosphorylation in neurons with successive neuronal demise⁴. Emphasizing the importance of neuronal energy metabolism in disease progression, a number of monogenic mitochondrial and neurometabolic disorders present as radiological or clinical MS phenocopies⁵. Moreover, several different neuronal ion channels, such as acid-sensing ion channel 1 (ASIC1), transient receptor potential cation channel subfamily M member 4 (TRPM4) and voltage-gated sodium channel subunit alpha Nav1.2 and Nav1.6 show enhanced activity during CNS inflammation^{6–8}. Together with excess accumulation of the excitatory neurotransmitter glutamate and a lowered pH, these ion channels contribute to inflammation-induced neuronal damage². However, after neuronal sensing of the inflammatory environment, the consecutive steps involving downstream gene expression changes that eventually determine neuronal fate are entirely unexplored⁹.

Methodologically, recording neuronal signatures in vivo has been challenging because it requires the isolation of intact neurons from a mixed CNS tissue. Furthermore, inflamed CNS samples are heavily contaminated by infiltrating immune cells, which bring their own transcriptional profile¹⁰. A recently described method circumvents these problems by using a rapid and direct affinity purification of polyribosomal RNA from genetically targeted cell types. Translating ribosome affinity purification (TRAP)¹¹ allows the isolation and profiling of cell-specific translated messenger RNA (mRNA) from whole tissues. TRAP and similar techniques have been successfully used to identify neuronal responses in patients undergoing antidepressant treatment¹², in anxiety-related

¹Institut für Neuroimmunologie und Multiple Sklerose, Zentrum für Molekulare Neurobiologie Hamburg, Universitätsklinikum Hamburg-Eppendorf, Hamburg, Germany. ²Zentrum für Molekulare Neurobiologie Hamburg, Universitätsklinikum Hamburg-Eppendorf, Hamburg, Germany. ³Leibniz-Institute für Neurobiologie, Magdeburg, Germany. ⁴Psychiatrische und Psychotherapeutische Klinik, Universitätsklinikum Erlangen, Friedrich-Alexander-Universität Erlangen-Nürnberg, Erlangen, Germany. ⁵Institut für Neuropathologie, Universitätsmedizin Göttingen, Georg-August-Universität Göttingen, Göttingen, Germany. ⁶Transkriptomanalyselabor, Institut für Entwicklungsbiologie, Universitätsmedizin Göttingen, Georg-August-Universität Göttingen, Göttingen, Germany. ⁷Center for Behavioral Brain Sciences and Medical Faculty, Otto von Guericke Universität, Magdeburg, Germany. ⁸Department of Pathology and Immunology, Service of Clinical Pathology, Geneva Faculty of Medicine, Geneva, Switzerland. ⁹These authors contributed equally: Benjamin Schattling, Jan Broder Engler. *e-mail: manuel.friese@zmn.uni-hamburg.de

disorders¹³ and in mouse models of fragile X syndrome¹⁴, amyotrophic lateral sclerosis¹⁵ and Parkinson's disease¹⁶. Therefore, this method is a promising approach to overcome the obstacles in inflamed CNS tissue underscored earlier and could deliver valuable insights into the overall neuronal reaction to inflammation.

In this study, we set out to systematically record neuron-intrinsic responses to inflammation to identify targetable neurodegenerative pathways. We demonstrate that targeted mRNA profiling using TRAP is suited to record a comprehensive picture of changes in neuronal gene expression under inflammatory challenge *in vivo*. It enabled us to successfully recover neuronal signals that could not have been identified in bulk samples because of the high background from other CNS-resident and CNS-infiltrating cell populations. Hence, we discovered the upregulation and accumulation of presynaptic protein bassoon (Bsn) in neuronal somata during inflammation in mice. Importantly, we could also detect somatic BSN accumulation in neurons in human MS tissue. Such Bsn accumulation exhibited a strong neurotoxic potential and could be successfully antagonized by pharmacological proteasome activation. Our findings of toxic Bsn proteinopathy in MS are reminiscent of disease pathways found in primary neurodegenerative disease with intracellular protein deposits¹⁷.

Results

Neuronal profiling during CNS inflammation. For targeted profiling of neurons during CNS inflammation, we isolated ribosome-bound mRNA from *Chat-L10a-eGFP* transgenic mice that express a fusion of enhanced green fluorescent protein (eGFP) and 60S ribosomal protein L10a under the choline O-acetyltransferase (*Chat*) promoter (Supplementary Fig. 1a) via TRAP. We chose *Chat*⁺ spinal motor neurons as target cells because they are directly injured during experimental autoimmune encephalomyelitis (EAE), the animal model of MS; therefore, they can reveal inflammation-induced response pathways *in vivo* (Supplementary Fig. 1b). We sampled five biological replicates of whole spinal cord and motor neurons under healthy and inflammatory conditions in the acute phase of EAE (day 12 postimmunization; Fig. 1a). After ensuring high consistency of the acquired dataset using principal component analysis (PCA) and unsupervised clustering (Supplementary Fig. 1c,d), we explored the relative contribution of transcripts from CNS-resident and CNS-infiltrating cells. To this end, we compiled sets of marker genes for immune cells, astrocytes, oligodendrocytes and neurons from the literature (Supplementary Table 1) and used them as the input for gene set enrichment analysis (GSEA)¹⁸. While the signatures from the immune cells and astrocytes were enriched in inflamed whole spinal cords, those from oligodendrocytes and neurons were depleted (Fig. 1b and Supplementary Table 2). Consequently, genes upregulated in inflamed spinal cords were heavily dominated by immune system transcripts that obscured changes in neuronal profiles (Supplementary Fig. 2a–d and Supplementary Table 3).

Markedly, TRAP from inflamed spinal cords resulted in a specific enrichment of neuronal signals and efficient clearance of signals from other cell types (Fig. 1c). However, direct comparison of inflamed and healthy motor neurons yielded several genes that have previously been assigned to immune system processes (Supplementary Fig. 3a–d). These could represent residual contamination by transcripts from invading immune cells or genuine immune genes, which were induced in the inflamed neurons themselves¹⁹. Since we were specifically interested in neuron-restricted response patterns, we devised a conservative filtering approach to focus our analysis on genes that were enriched by TRAP and changed by inflammation (Supplementary Fig. 3e,f). Following this approach, we identified 354 up- and 448 downregulated candidate genes, which showed a strong inflammation-induced regulation in motor neurons (Fig. 1d and Supplementary Table 3). Only a small

fraction of these genes was annotated as immune system-related (Supplementary Fig. 3g).

To explore the biological meaning of the overall changes in gene expression in inflamed motor neurons, we performed overrepresentation analysis of biological process gene ontology (GO) terms and visualized the results as enrichment maps²⁰. This analysis yielded multiple clusters of GO terms indicating a downregulation of genes involved in ATP synthesis and electron transport chain (Fig. 1e, Supplementary Fig. 4a and Supplementary Table 4), changes that might aggravate neuronal energy shortage³. Notably, we also found an overrepresentation of genes involved in protein breakdown pathways including ubiquitin- and proteasome-dependent protein degradation (Fig. 1e and Supplementary Fig. 4b), which could indicate an increased demand to clear damaged or misfolded neuronal proteins, as observed in primary neurodegenerative diseases¹⁷.

Neuroinflammation results in neuronal Bsn accumulation in mice and humans. Next, we sought to extract promising targets for further mechanistic and therapeutic studies. Since the foremost aim was to translate our findings to human patients, we were specifically interested in upregulated neuronal candidate genes that could be validated in the chronic degenerative CNS plaques of patients with MS. Therefore, we used a published microarray dataset of autopsy brain samples²¹ and compared chronic and chronic active MS plaques versus unaffected control tissue. Of our 354 upregulated neuronal candidate genes, 39 (approximately 11%) were also induced in chronic human MS plaques (Fig. 2a). Among these, the bassoon presynaptic cytomatrix protein (*Bsn*) gene represented the most significant hit in both datasets (Fig. 2b and Supplementary Table 5), showing a robust induction in inflamed motor neurons and MS plaques (Fig. 2c and Supplementary Fig. 5a). Although we consider all identified proteins as strong candidates with potential roles in MS pathology, we further focused on Bsn for detailed analysis and validated the induction of Bsn in a second independent TRAP cohort (Supplementary Fig. 5b).

To assess Bsn induction on the protein level, we performed immunohistochemical staining of mouse spinal cord sections. Remarkably, we observed a massive accumulation of Bsn protein in neuronal somata during inflammation in acute (Fig. 2d, day 14 postimmunization) and chronic EAE (Supplementary Fig. 5c, day 30 postimmunization), but not in controls immunized with complete Freund's adjuvant (CFA) without myelin-oligodendrocyte glycoprotein 35–55 (MOG_{35–55}) peptide (Supplementary Fig. 5d). Bsn staining of inflamed neurons appeared homogeneously distributed throughout the cell body at high exposures that allowed the capture of physiological, synaptic staining in healthy controls (Fig. 2d). However, at low exposures it was primarily characterized by punctate somatic staining (Supplementary Fig. 5e).

Somatic localization was unexpected because under physiological conditions Bsn is restricted to presynaptic boutons^{22,23}. We further investigated whether somatic mislocalization could be a general phenomenon of presynaptic proteins under inflammatory conditions. However, presynaptic localization of synapsins was preserved during CNS inflammation (Supplementary Fig. 5f), underscoring that inflammation-induced somatic accumulation was not a general feature of presynaptic proteins.

To verify the translatability of our findings to human disease, we stained spinal cord specimens of patients with MS with varying inflammatory activity (Supplementary Fig. 6a and Supplementary Table 6) compared to individuals without MS for BSN deposits. Indeed, we detected increased numbers of BSN⁺ neuronal somata in MS specimens showing punctate somatic staining (Fig. 2e). This was not observed in control staining, where primary antibody was omitted (Supplementary Fig. 6b). In some areas of the MS specimens, up to 80% of microtubule-associated protein 2 (MAP2)⁺ neurons were affected by somatic BSN deposits (Supplementary Fig. 6c). We further

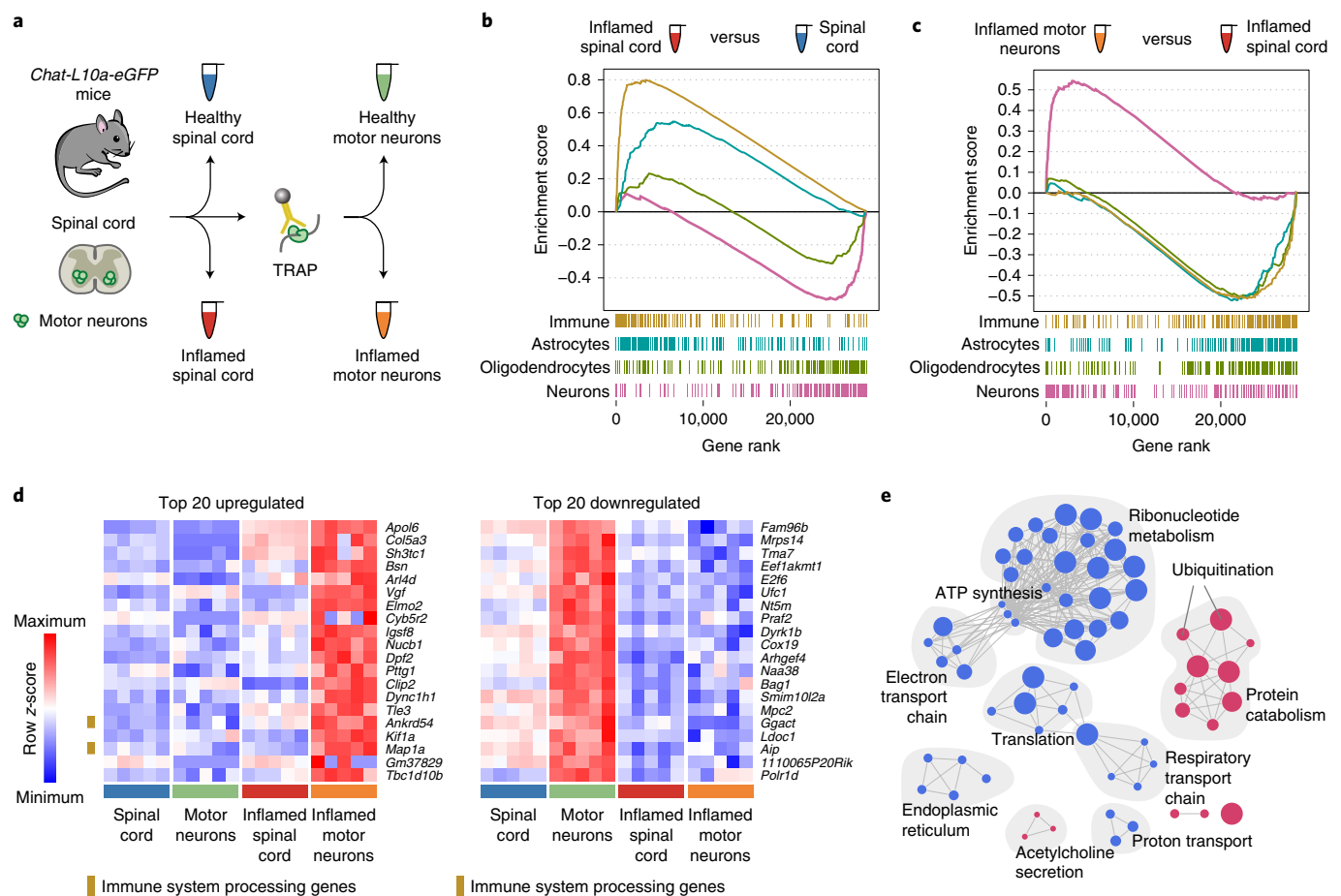


Fig. 1 | Expression profiling of neurons during CNS inflammation. **a**, Diagram of experimental approach. **b**, GSEA of marker genes from indicated cell populations in inflamed spinal cord versus healthy spinal cord. GSEA adjusted for multiple comparisons by FDR. **c**, GSEA of marker genes in inflamed motor neurons versus inflamed spinal cord. GSEA adjusted for multiple comparisons by FDR. **d**, Gene expression heatmap of top 20 up- and downregulated motor neuron candidate genes. Genes annotated for 'immune system processing' are marked in orange-brown on the left. Candidates were identified by DESeq2, using negative binomial generalized linear models and adjusted for multiple comparisons by FDR: $n = 5$ biologically independent samples per group each pooled from 3 mice, $\log_2(\text{fold change}) > 1$; FDR-adjusted $P < 0.05$. **e**, Enrichment map of regulated biological process GO terms generated from candidate genes. Red, upregulated; blue, downregulated; node size, gene set size; gray lines, gene set overlap.

realized that the amino acid sequence of BSN is characterized by a high percentage of intrinsically disordered residues (92.11% in mouse Bsn and 90.75% in human BSN; Supplementary Fig. 6d) that indicate a lack of fixed tertiary protein structure²⁴. This observation, together with the notable size of Bsn (419 kDa), might support the notion of an unstable native protein fold resulting in a propensity to form deposits under an inflammatory challenge.

Altogether, we found that neuroinflammation triggers neuronal Bsn induction and accumulation in mice and humans. This mislocalization of Bsn and its potential to participate in protein accumulation suggests a thus-far-unrecognized pathological role during inflammation-induced neurodegeneration.

Bsn accumulation results in cellular toxicity. To investigate the consequence of somatic Bsn accumulation, we first overexpressed eGFP-Bsn in comparison to eGFP in mouse Neuro-2a (N2a) cells. In contrast to the homogeneous distribution of eGFP, we observed a punctate cytosolic accumulation of eGFP-Bsn, reminiscent of our in vivo findings in EAE and MS (Fig. 3a). In contrast, overexpression of microtubule-associated protein 1A (MAP1a), another large synaptic protein (300 kDa) that was induced in inflamed motor neurons during EAE and in MS plaques (Fig. 2b), did not result in punctate cytosolic accumulation (Supplementary Fig. 7a).

Moreover, eGFP-Bsn overexpression was accompanied by a 40% reduction in cellular survival supporting the toxic effect of Bsn deposits (Fig. 3b). Because we observed a high cell-to-cell variability in eGFP-Bsn expression, we took advantage of single-cell RNA sequencing (RNA-seq)²⁵ to resolve genome-wide expression changes that were driven by the gradual increase of the eGFP-Bsn load. The resulting dataset comprised of 468 single cells that were ordered along a pseudotime trajectory²⁶, starting from cells with low eGFP-Bsn expression and gradually progressing to cells with high eGFP-Bsn expression. The genes driven by this trajectory indicated a downregulation of biosynthesis and energy metabolism, while protein catabolism and unfolded protein response (UPR) were induced (Fig. 3c,d). UPR induction was also accompanied by colocalization of eGFP-Bsn and the endoplasmic reticulum marker protein disulfide isomerase (PDI; Supplementary Fig. 7b), which might indicate endoplasmic reticulum retention—a potent UPR trigger²⁷. Furthermore, we found a branching of the pseudotime trajectory, indicating that cells with a high eGFP-Bsn load either passed to apoptosis or managed to uphold energy metabolism (Fig. 3e). These findings resembled the in vivo EAE signatures (Supplementary Fig. 7c,d and Supplementary Table 7) and raised the possibility that Bsn accumulation might be a driving force of the inflammation-induced neuronal response pattern.

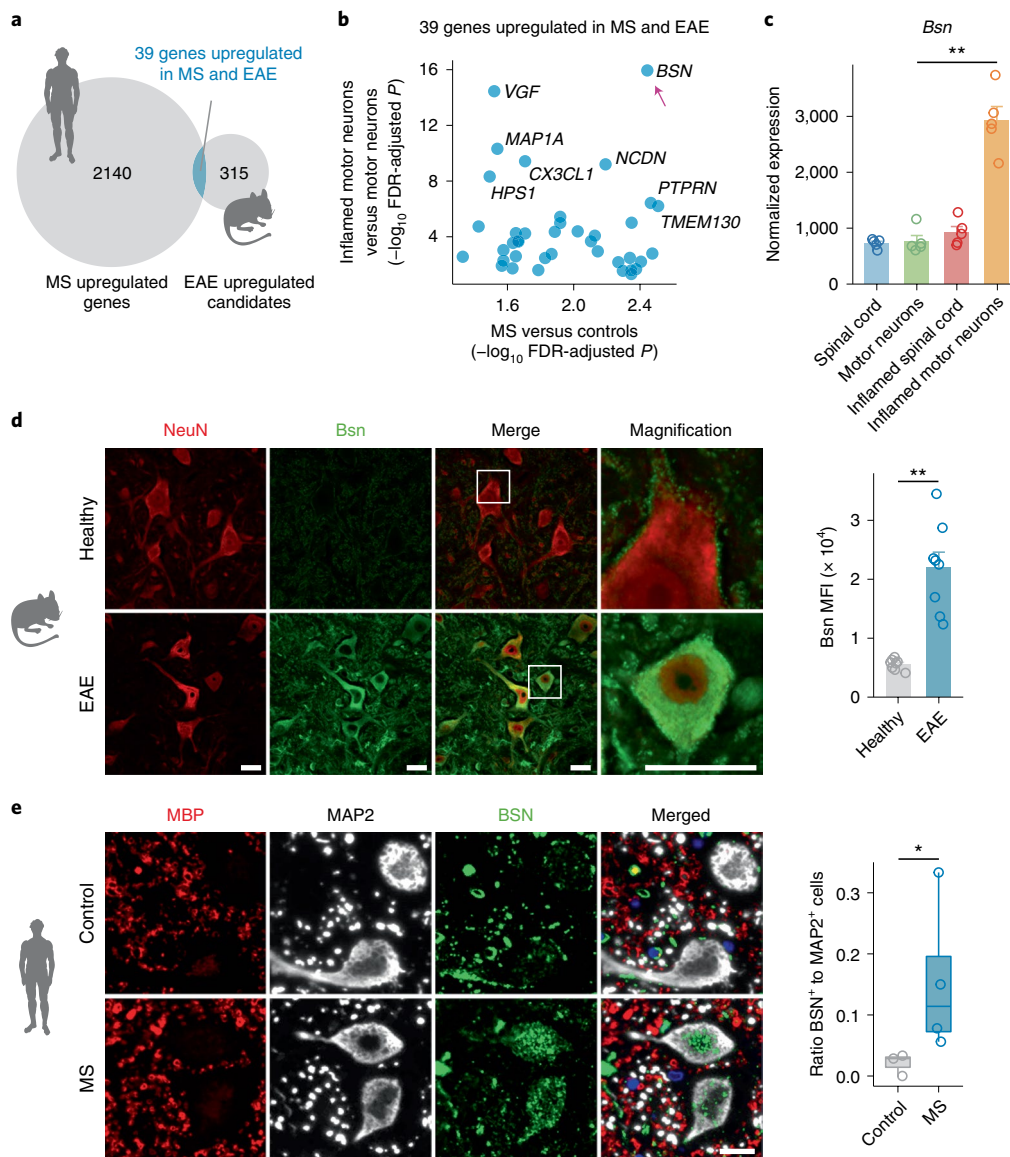


Fig. 2 | BSN accumulates in neuronal somata in EAE and MS. **a**, Venn diagram showing the overlap between genes upregulated in MS plaques²¹ and upregulated candidates from the TRAP EAE screen. **b**, Scatter plot of statistical significance of overlapping genes in MS plaque versus control and inflamed motor neurons versus motor neurons. Candidates were identified by DESeq2, using negative binomial generalized linear models adjusted for multiple comparisons by FDR; $n=5$ biologically independent samples per group, each pooled from 3 mice for the mouse dataset, $n=2$ controls versus $n=4$ MS samples for the published human dataset, $\log_2(\text{fold change}) > 1$, FDR-adjusted $P < 0.05$. **c**, Normalized RNA-seq expression of *Bsn* in the spinal cord, inflamed spinal cord, motor neurons and inflamed motor neurons. Statistical testing by DESeq2, using negative binomial generalized linear models adjusted for multiple comparisons by FDR; $n=5$ biologically independent samples per group, each pooled from 3 mice, motor neurons versus inflamed motor neurons; $P = 1.14 \times 10^{-16}$. The bars show mean values \pm s.e.m. **d**, Immunohistochemical staining of *Bsn* in cervical spinal cord sections of healthy and acute EAE mice (day 14 postimmunization). Co-staining for neurons (NeuN). Two-tailed Student's t -test; $t(14) = 6.12$, $P < 0.0001$; $n=8$ mice per group. The bars show mean values \pm s.e.m. MFI, mean fluorescence intensity. Scale bar, 20 μm . **e**, Immunohistochemical staining of BSN in spinal cord sections of controls and patients with MS. Co-staining for myelin via MBP and neurons via MAP2. One-tailed Mann-Whitney U -test. $n=3$ controls versus $n=4$ patients with MS, $P = 0.0286$. The boxplots show the median and interquartile range. Scale bar, 40 μm . * $P < 0.05$; ** $P < 0.01$.

To further investigate *Bsn* toxicity in vivo, we transgenically expressed *Bsn* in *Drosophila melanogaster* neurons, which do not possess a direct *Bsn* homolog²⁸. We engineered two transgenic lines with *Bsn* downstream of the upstream activating sequences (UAS) and used the pan-neuronal embryonic lethal abnormal vision (*Elav*) promoter to drive the Gal4 activator (*Elav-Gal4*), which in turn drives *Bsn* expression (Fig. 4a). Following this approach, we generated two fly lines possessing either low or high *Bsn* expression in neurons and termed them *UAS-Bsn*^{low} and *UAS-Bsn*^{high}, respectively (Fig. 4b). Resembling our previous results in EAE mice, human

MS and *Bsn*-transfected N2a cells, *Bsn* staining showed a punctate cytosolic accumulation in neurons (Fig. 4b). Consistently, in both *UAS-Bsn*^{low} and *UAS-Bsn*^{high} flies we observed significantly reduced retinal thickness, which shows cellular neurodegeneration (Fig. 4c). Moreover, *UAS-Bsn*^{low} and *UAS-Bsn*^{high} flies presented with a motor deficit that resulted in reduced climbing ability (Fig. 4d). Finally, transgenic *Bsn* expression led to a significant dose-dependent reduction in the lifespan of *Drosophila* compared to the *Elav-Gal4* control line (Fig. 4e), together supporting the neurotoxic effect of somatic *Bsn* accumulation in vivo.

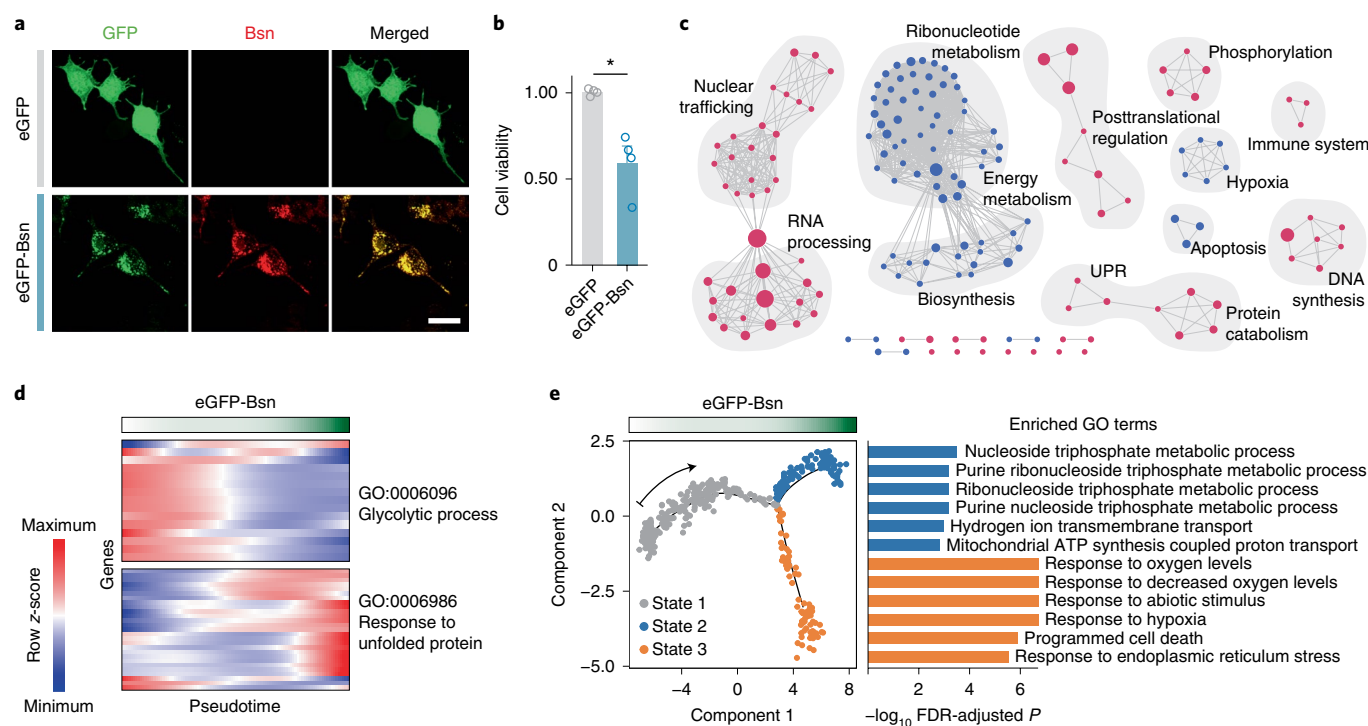


Fig. 3 | Bsn accumulation is neurotoxic. a, Immunocytochemical staining of Bsn in N2a cells overexpressing eGFP-Bsn or eGFP alone. The experiment was repeated four times with similar results. Scale bar, 20 μ m. **b**, Viability of N2a cells 72 h after transfection. Two-tailed, one-sample *t*-test against controls normalized to 1; $t(3) = 4.14$, $P = 0.0256$. $n = 4$ independent experiments. The bars show mean values \pm s.e.m. **c**, Enrichment map of regulated biological process GO terms driven by Bsn expression in single-cell RNA-seq of N2a cells overexpressing eGFP-Bsn. Red, upregulated; blue, downregulated; node size, gene set size; gray lines, gene set overlap. **d**, Gene expression heatmap of genes belonging to the indicated GO terms plotted against pseudotime, representing 468 cells ordered by increasing Bsn expression in single-cell RNA-seq of N2a cells overexpressing eGFP-Bsn. **e**, Branching point analysis of pseudotime trajectory driven by Bsn expression. Two identified branches were characterized by GO term enrichment analysis. The top six significant GO terms for each branch are shown with their respective FDR-adjusted *P* values. GSEA adjusted for multiple comparisons by FDR; $n = 468$ cells from one experiment. * $P < 0.05$.

Bsn deletion protects against inflammation-induced neurodegeneration. Next, we elucidated the role of Bsn in the same inflammatory model we used for the initial identification of inflammation-induced neuronal responses. For this purpose, we used *Bsn* knockout mice²⁹ (*Bsn*^{-/-}; Fig. 5a) and subjected these mice to EAE compared to wild-type littermates. After reaching comparable maximum scores in the acute phase, *Bsn*^{-/-} mice showed a significantly better recovery from clinical disability compared to their wild-type littermates (Fig. 5b). This was accompanied by significantly better preservation of axons and neurons in the chronic phase of EAE (Fig. 5c,d) and was preceded by significantly reduced numbers of APP⁺-injured axons already in the acute phase (Fig. 5e). Of note, baseline counts of axons and neurons were comparable between *Bsn*^{-/-} mice and their littermate controls (Supplementary Fig. 8a,b). Moreover, the number of inflammatory lesions and the densities of infiltrating CD3⁺ T cells and Mac-3⁺ macrophages were similar to wild-type littermates (Fig. 5e), and the subset composition of infiltrating T cells was comparable (Supplementary Fig. 8c,d). Together, these findings argue against a deficit of immune cell activation and infiltration in *Bsn*^{-/-} mice and show a critical contribution of Bsn to inflammation-induced neuroaxonal injury.

Pharmacological proteasome activation clears Bsn deposits and protects neurons. Following the notion that Bsn might exert its pathological function via somatic accumulation, we reasoned that activation of the protein degradation machinery might clear Bsn deposits and enhance neuronal survival. To test this hypothesis, we used the ubiquitin carboxyl-terminal hydrolase 14 (USP14) inhibitor IU1³⁰, which has been previously shown to increase proteasome

activity in the CNS after systemic administration³¹. USP14 is a deubiquitylating enzyme (DUB) and inhibits proteasomal degradation of ubiquitin-protein conjugates by trimming ubiquitin chains on protein substrates before their degradation. Since Bsn has been shown to be ubiquitinated in the CNS³², we reasoned that USP14 inhibition would accelerate its degradation. To minimize a possible effect of IU1 on the initial immune activation and infiltration, we started IU1 treatment at day 8 after EAE immunization, a time point when the animals had already started to develop neurological symptoms. Strikingly, IU1 treatment led to a marked reduction of Bsn accumulation in neuronal somata during EAE, partially restoring the physiological presynaptic localization of Bsn (Fig. 6a). This was accompanied by a significantly better recovery of IU1-treated mice from clinical disability compared to vehicle-treated controls (Fig. 6b). The protective effect of IU1 was also seen at the cellular level, leading to a better preservation of axons and neurons during the chronic phase of EAE (Fig. 6c,d). Notably, immune cell infiltration and T cell subset composition was unchanged in these experiments (Fig. 6e and Supplementary Fig. 8e), supporting the notion of a neuroprotective mode of action of IU1.

Neuronal aggresome formation during inflammation is Bsn-dependent. Since several lines of evidence suggested that CNS inflammation induces the generation of neurotoxic Bsn aggregates, we finally assessed aggresome formation in spinal cord motor neurons by staining them with the thioflavin T derivative, Proteostat. Notably, aggresome numbers were induced by EAE, partially rescued by IU1 treatment and completely abolished in *Bsn*^{-/-} animals (Fig. 7). These data establish Bsn as a necessary prerequisite for

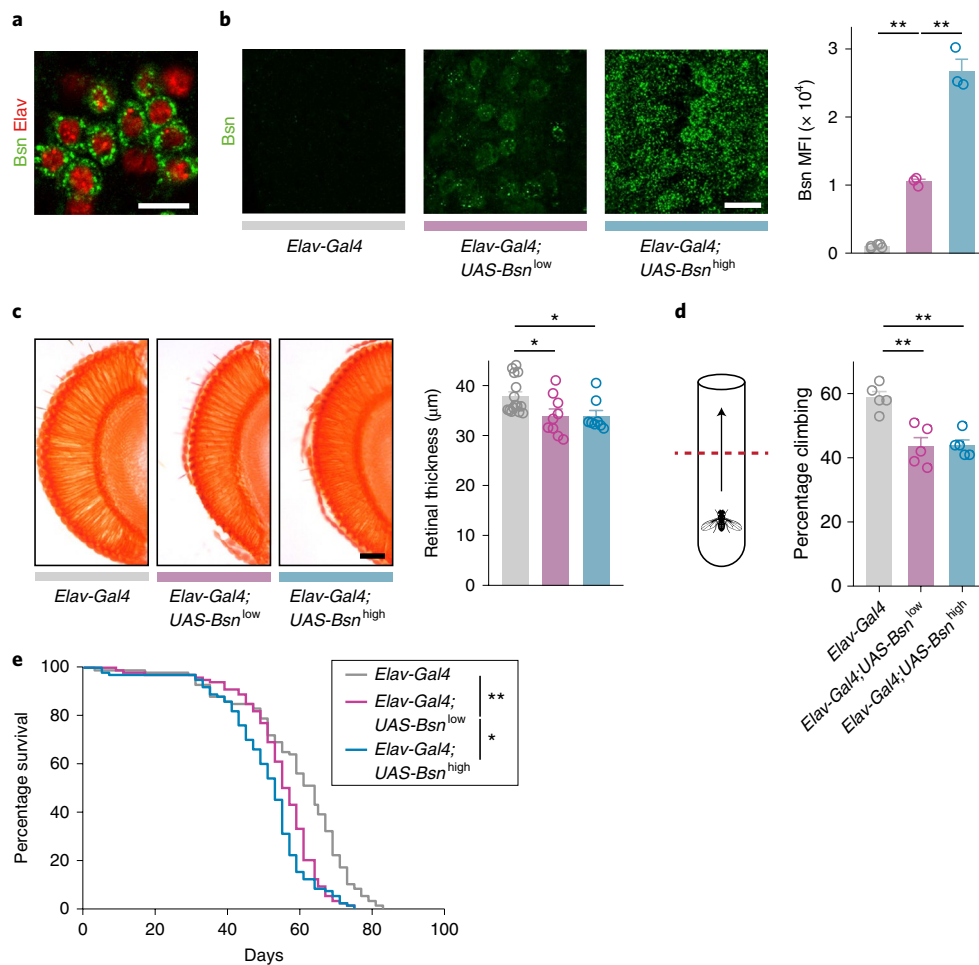


Fig. 4 | Somatic Bsn expression causes neurodegeneration and reduces lifespan in *Drosophila*. **a**, Representative immunohistochemical staining of Bsn in *Elav-Gal4;UAS-Bsn^{high}* flies. Co-staining for neurons (Elav). The experiment was repeated three times with similar results. Scale bar, 20 μ m. **b**, Immunohistochemical staining of Bsn in the ventral nerve cords of *D. melanogaster* larvae expressing Bsn under the control of the neuronal driver *Elav*. The control line *Elav-Gal4* and the independent lines *Elav-Gal4;UAS-Bsn^{low}* and *Elav-Gal4;UAS-Bsn^{high}* are shown and quantified (one-way ANOVA with Šidák's post hoc test: $n = 5$ *Elav-Gal4*, $n = 3$ *Elav-Gal4;UAS-Bsn^{low}*, $n = 3$ *Elav-Gal4;UAS-Bsn^{high}* larvae; $F_{(2,8)} = 258.1$, $P < 0.0001$. Šidák's post hoc test: *Elav-Gal4* versus *Elav-Gal4;UAS-Bsn^{low}*, $P < 0.0001$; *Elav-Gal4;UAS-Bsn^{low}* versus *Elav-Gal4;UAS-Bsn^{high}*, $P < 0.0001$). The bars show mean values \pm s.e.m. MFI, mean fluorescence intensity. Scale bar, 20 μ m. **c**, Histopathological staining of retinal sections at day 30 with quantification of retinal thickness (one-way ANOVA with Šidák's post hoc test: $n = 15$ *Elav-Gal4*, $n = 9$ *Elav-Gal4;UAS-Bsn^{low}*, $n = 8$ *Elav-Gal4;UAS-Bsn^{high}* flies; $F_{(2,29)} = 4.617$, $P = 0.0182$. Šidák's post hoc test: *Elav-Gal4* versus *Elav-Gal4;UAS-Bsn^{low}*, $P = 0.0339$; *Elav-Gal4* versus *Elav-Gal4;UAS-Bsn^{high}*, $P = 0.0377$). The bars show mean values \pm s.e.m. Scale bar, 20 μ m. **d**, Assessment of climbing ability at day 30 with quantification (one-way ANOVA with Šidák's post hoc test: $n = 5$ vials with 10 flies each per group; $F_{(2,12)} = 16.55$, $P = 0.0004$, Šidák's post hoc test: *Elav-Gal4* versus *Elav-Gal4;UAS-Bsn^{low}*, $P = 0.0006$; *Elav-Gal4* versus *Elav-Gal4;UAS-Bsn^{high}*, $P = 0.0007$). The bars show mean values \pm s.e.m. **e**, Lifespan assay with quantification. One representative experiment of two with similar results is shown (Mantel-Cox log-rank test. $n = 100$ flies per group. *Elav-Gal4* versus *Elav-Gal4;UAS-Bsn^{low}*, $P < 0.0001$; *Elav-Gal4;UAS-Bsn^{low}* versus *Elav-Gal4;UAS-Bsn^{high}*, $P = 0.0237$). The bars show mean values \pm s.e.m. * $P < 0.05$; ** $P < 0.01$.

inflammation-induced aggresome formation, but also show that pharmacological proteasome activation can either halt aggresome formation or trigger aggresome clearance.

Discussion

Despite the urgent need to better understand neuronal injury during inflammation, systems biology approaches addressing this topic have been sparse. One reason for this is the strong contamination of inflamed tissues by immune cell transcripts, which requires a technique to specifically extract neuronal signals. In this study, we used cell type-specific isolation of translating ribosomes (TRAP) to record a comprehensive snapshot of inflammation-exposed motor neurons during EAE. Thereby, we could identify 354 up- and 448 downregulated neuronal candidate genes (Fig. 1d), only about 5% of which would have been identified by whole tissue analysis. We

consider this dataset a valuable and rich resource for exploring the mechanistic underpinning of neuronal injury and resistance in response to inflammation.

One of the central pathways that was deregulated by inflammation in neurons is energy metabolism. This is reflected in groups of GO terms concerning 'ATP synthesis', 'electron transport chain', 'respiratory transport chain' and 'proton transport', but also 'ribonucleotide metabolism', which subsumes a number of ADP/ATP catabolizing enzymes. These GO terms were driven by the downregulation of transcripts encoding integral components across all mitochondrial respiratory chain complexes (Fig. 1e and Supplementary Fig. 4a), which are the molecular backbone of oxidative phosphorylation. Moreover, a number of genes encoding mitochondrial ribosomal proteins that are essential for local mitochondrial translation of mitochondrial DNA-encoded oxidative phosphorylation components

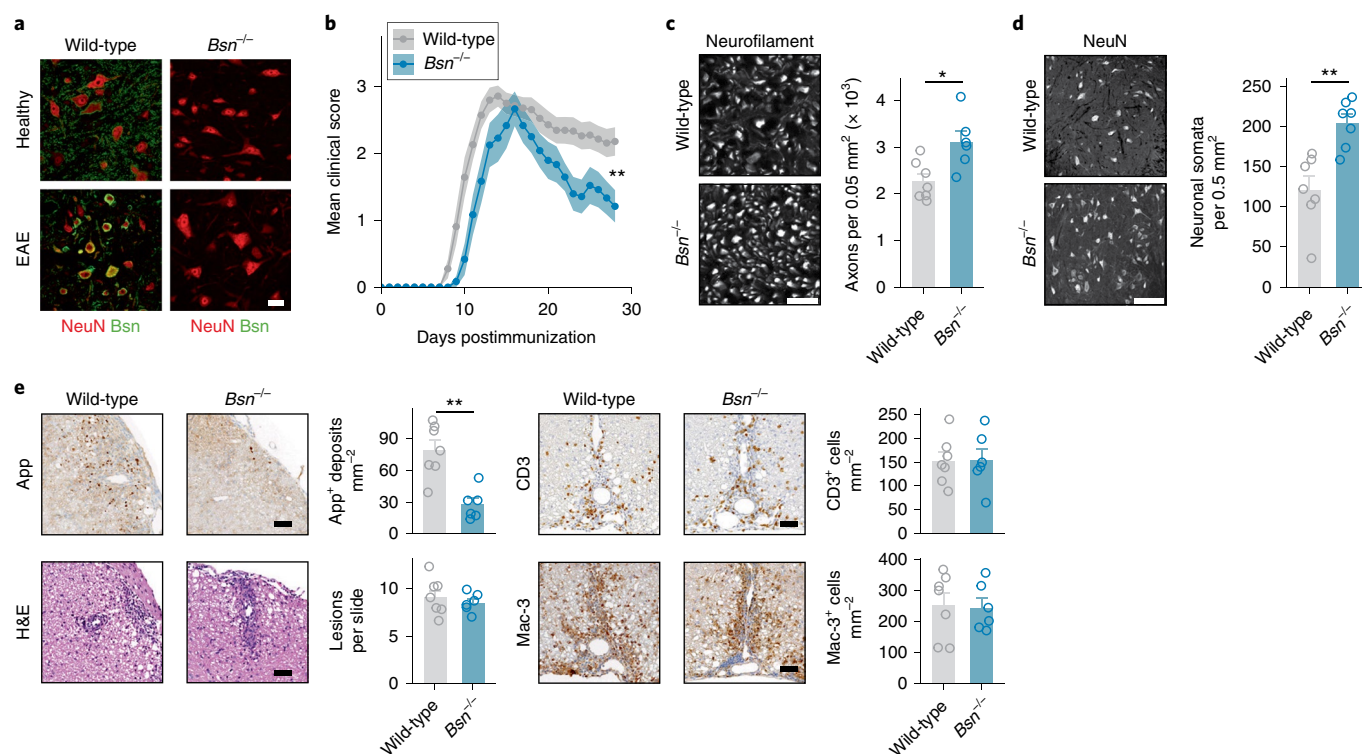


Fig. 5 | *Bsn* drives neuroaxonal injury and clinical disability in EAE. **a**, Immunohistochemical staining of Bsn in cervical spinal cord sections of wild-type and *Bsn*^{-/-} mice in a healthy state and during acute EAE (day 16 postimmunization). Co-staining for neurons (NeuN). The experiment was repeated three times with similar results. Scale bar, 20 μ m. **b**, Clinical scores of wild-type and *Bsn*^{-/-} mice undergoing EAE. Data are pooled from two independent experiments (two-tailed Mann-Whitney *U*-test of the area under the curve; $n = 21$ wild-type versus $n = 12$ *Bsn*^{-/-} mice, $P = 0.0023$). Mean values \pm s.e.m. are shown. **c**, Immunohistochemical staining and quantification of surviving neurofilament-positive axons in the dorsal columns of cervical spinal cord sections of wild-type and *Bsn*^{-/-} mice at day 28 postimmunization. Data are pooled from two independent experiments (two-tailed Student's *t*-test; $n = 7$ wild-type versus $n = 6$ *Bsn*^{-/-} mice; $t(11) = 3.009$, $P = 0.0119$). The bars show mean values \pm s.e.m. Scale bar, 10 μ m. **d**, Immunohistochemical staining and quantification of surviving NeuN⁺ neurons in cervical spinal cord sections of wild-type and *Bsn*^{-/-} mice at day 28 postimmunization. Data are pooled from two independent experiments (two-tailed Student's *t*-test; $n = 7$ wild-type versus $n = 7$ *Bsn*^{-/-} mice; $t(12) = 4.124$, $P = 0.0014$). The bars show mean values \pm s.e.m. Scale bar, 100 μ m. **e**, Histopathological staining and quantification of injured amyloid- β precursor protein (App)⁺ axons, inflammatory lesions (H&E staining), T cells (CD3) and macrophages (Mac-3) in cervical spinal cord sections of wild-type and *Bsn*^{-/-} mice at day 15 postimmunization. Data are pooled from two independent experiments (two-tailed Student's *t*-test; $n = 7$ wild-type versus $n = 6$ *Bsn*^{-/-} mice; App, $t(11) = 4.424$, $P = 0.0010$; H&E, $t(11) = 0.8105$, $P = 0.4348$; CD3, $t(11) = 0.0444$, $P = 0.9653$; MAC-3, $t(11) = 0.1696$, $P = 0.8684$). The bars show mean values \pm s.e.m. Scale bar, 50 μ m. * $P < 0.05$; ** $P < 0.01$.

were downregulated, including mitochondrial ribosomal protein S7 (*Mrps7*; Fig. 1e and Supplementary Fig. 4a). Homozygous missense mutation of human *MRPS7* has been associated with deficiency in mitochondrial protein synthesis, complex I and IV activity and rate of ATP production, resulting in a severe familial form of combined oxidative phosphorylation deficiency³³. Thus, during neuroinflammation cellular respiration in neurons potentially suffers from both withdrawal of nuclear-encoded oxidative phosphorylation transcripts and reduced mitochondrial protein synthesis capacity. Together, this profile is consistent with a severely disturbed neuronal energy metabolism, a feature previously linked to neurodegeneration in different contexts, including MS^{3,34}.

Another pathway upregulated in neurons during inflammation is protein degradation, including 'protein ubiquitination' and 'ubiquitin-dependent protein catabolism' by the ubiquitin-proteasome system (UPS; Fig. 1e and Supplementary Fig. 4b). The UPS is a complex system that targets proteins by ubiquitination and then loads them into the proteasome for proteolytic degradation. It is a mechanism to protect the cell against exuberant protein load as well as damaged, misfolded or aggregated proteins³⁵. Moreover, UPS induction can frequently be found in primary neurodegenerative diseases where accumulating ubiquitinated protein species reflect

a global collapse of protein homeostasis¹⁷. The particular vulnerability of the cellular network that maintains protein homeostasis in response to stressors³⁶, makes it plausible that neuroinflammation could trigger toxic protein deposition³⁷ in a similar manner as tau and α -synuclein^{38,39}.

For further mechanistic studies, we focused on *Bsn* as one of our top five upregulated candidate genes. We chose *Bsn* because we found it equally induced in a published microarray dataset of chronic and chronic active MS plaques²¹, potentially increasing the chance for successful translation into human MS (Fig. 2a,b). Indeed, we found both proteins—murine Bsn and human BSN—strongly induced in neuronal somata in EAE and MS, respectively (Fig. 2d,e). *Bsn* is a large multidomain protein (419 kDa) of the neuronal presynaptic cytoskeletal matrix, which consists of an N-terminal Zn²⁺ finger, a stretch of polyglutamine repeats and several piccolo-bassoon homology domains. *Bsn* expression appears very early during synaptogenesis at sites of active synaptic vesicle cycling and is a prominent component of active zone precursor vesicles, where it is thought to participate in orchestrating the events at the synapse³³. However, inflammatory signals, for example, cytokines or chemokines have thus far not been reported to regulate its expression. Because of its long stretches of intrinsically disordered

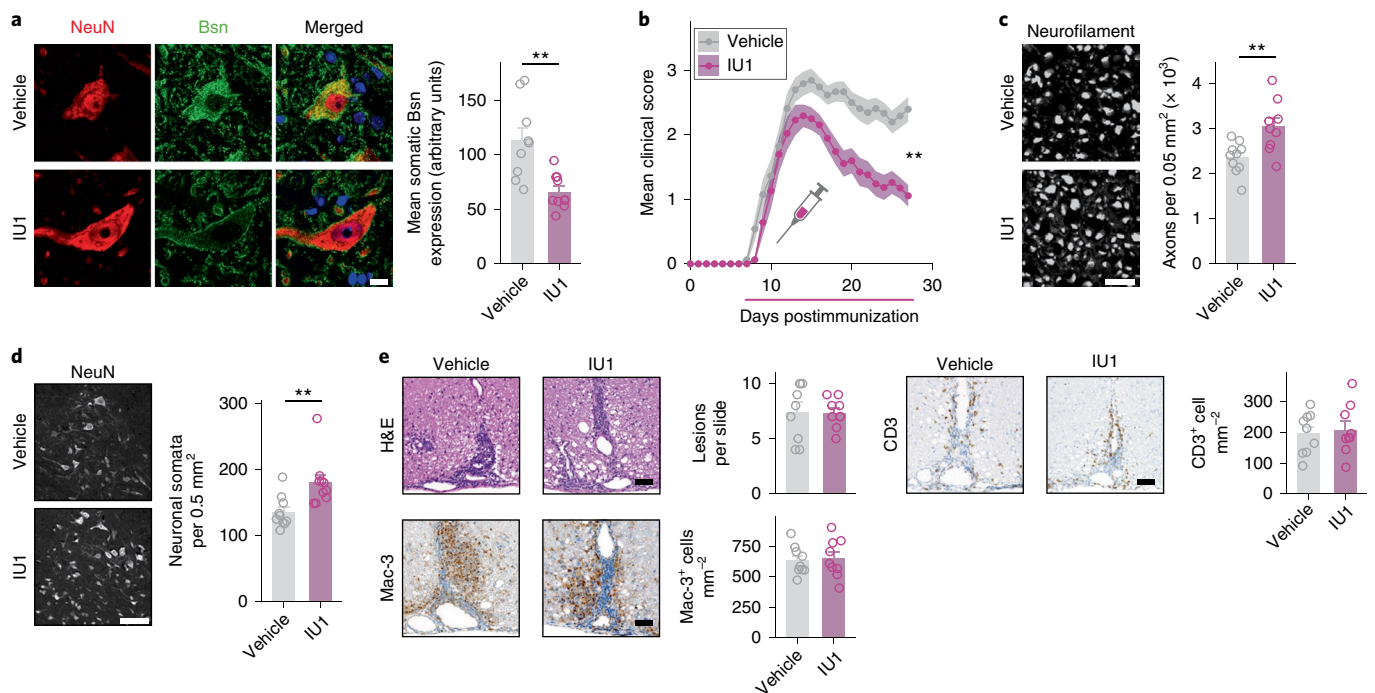


Fig. 6 | Pharmacological proteasome activation clears somatic Bsn accumulation and ameliorates neurodegeneration during CNS inflammation.

a, Immunohistochemical staining of NeuN and Bsn and quantification of somatic Bsn in cervical spinal cord sections of vehicle-treated and IU1-treated mice at day 27 postimmunization (two-tailed Student's *t*-test; $n=9$ vehicle-treated versus $n=10$ IU1-treated mice; $t(17)=3.773$, $P=0.0015$). The bars show mean values \pm s.e.m. Scale bar, 10 μ m. **b**, Clinical scores of vehicle-treated and IU1-treated mice undergoing EAE. Data are pooled from two independent experiments (two-tailed Mann-Whitney *U*-test of the area under the curve; $n=24$ vehicle-treated versus $n=23$ IU1-treated mice, $P=0.0005$). Mean values \pm s.e.m. are shown. **c**, Immunohistochemical staining and quantification of surviving neurofilament-positive axons in the dorsal columns of cervical spinal cord sections of vehicle-treated and IU1-treated mice at day 27 postimmunization. Data are pooled from two independent experiments (two-tailed Student's *t*-test; $n=10$ vehicle-treated versus $n=9$ IU1-treated mice; $t(17)=3.167$, $P=0.0056$). The bars show mean values \pm s.e.m. Scale bar, 10 μ m. **d**, Immunohistochemical staining and quantification of surviving NeuN⁺ neurons in cervical spinal cord sections of vehicle-treated and IU1-treated mice at day 27 postimmunization. Data are pooled from two independent experiments (two-tailed Student's *t*-test; $n=10$ vehicle-treated versus $n=10$ IU1-treated mice; $t(18)=3.206$, $P=0.0049$). The bars show mean values \pm s.e.m. Scale bar, 100 μ m. **e**, Histopathological staining and quantification of inflammatory lesions (H&E), T cells (CD3) and macrophages (Mac-3) in cervical spinal cord sections of vehicle-treated and IU1-treated mice at day 15 postimmunization. Data are pooled from two independent experiments (two-tailed Student's *t*-test; $n=9$ vehicle-treated versus $n=9$ IU1-treated mice; H&E, $t(16)=0.1159$, $P=0.9092$; CD3, $t(16)=0.3403$, $P=0.7381$; Mac-3, $t(16)=0.2716$, $P=0.7894$). The bars show mean values \pm s.e.m. Scale bar, 50 μ m. ** $P<0.01$.

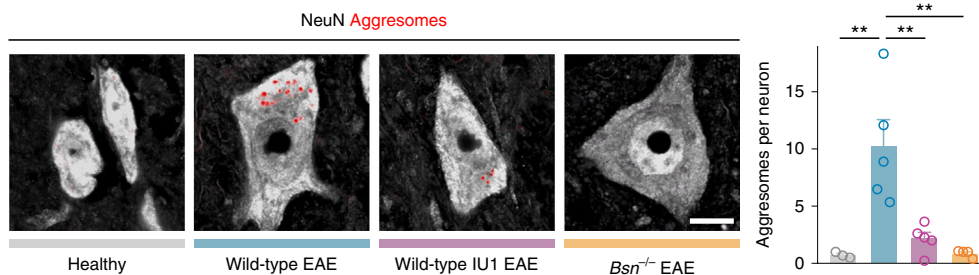


Fig. 7 | Neuronal aggresome formation during inflammation is Bsn-dependent. Immunohistochemical co-staining of NeuN and aggresomes in cervical spinal cord motor neurons with quantification at day 27–28 postimmunization. Healthy animals are compared to wild-type EAE, wild-type EAE with IU1 treatment (as in Fig. 6) and *Bsn*^{-/-} EAE. Data are pooled from two independent experiments (One-way ANOVA with Šidák's post hoc test; $n=3$ healthy versus $n=5$ wild-type EAE versus $n=5$ wild-type IU1 EAE versus $n=4$ *Bsn*^{-/-} EAE mice; $F_{(3,13)}=10.62$, $P=0.0008$. Šidák's post hoc test: healthy versus wild-type EAE, $P=0.0023$; wild-type EAE versus wild-type IU1 EAE, $P=0.0027$; wild-type EAE versus *Bsn*^{-/-} EAE, $P=0.0013$). The bars show mean values \pm s.e.m. ** $P<0.01$.

residues (Supplementary Fig. 6d), Bsn appears particularly prone to accumulation, which might be perpetuated by increased protein concentration as a consequence of induced expression and disturbed protein homeostasis⁴⁰. Intrinsically disordered residues

have been shown to facilitate pathological protein accumulation and can be found in several proteins that are associated with primary neurodegenerative diseases like amyloid- β protein, tau, α -synuclein and huntingtin¹⁷. Notably, human *BSN* mutations

have recently been associated with familiar and idiopathic forms of progressive supranuclear palsy-like syndromes, a neurodegenerative tauopathy clinically defined as atypical parkinsonism. Interestingly, the familiar mutation (p.P3866A) led to decreased Bsn solubility *in vitro*⁴¹.

While Bsn accumulation may conceivably lead to a loss of Bsn function via sequestration, it could also exert direct toxicity by interfering with other intracellular functions. It is likely that a combination of Bsn induction, its propensity to accumulate⁴² and its mislocalization to neuronal somata accounts for the toxic gain-of-function and subsequent neurodegenerative phenotype. Since Bsn has been shown to inhibit key factors of the UPS and autophagy-mediated lysosomal proteolysis, such as E3 ubiquitin-protein ligase SIAH1⁴³ and autophagy protein 5 (ATG5)⁴⁴, accumulated Bsn might directly interfere with these pathways and thereby undermine its own disposal.

When considering Bsn as a therapeutic target, it is important to determine any potential unwanted side effects of Bsn interference. While Bsn knockouts are viable, they possess a lowered threshold for kainic acid-induced epileptic seizures. Beyond that, the precise functional impact of Bsn depletion at an organismic level has not been systematically studied^{22,23}. Thus, therapeutic Bsn aggregate interference, for example, by specific antibodies as currently pursued in Alzheimer's and other neurodegenerative diseases⁴⁵, will require careful consideration. A probably more elegant approach involves the induction of mechanisms that are suited to support the clearance of Bsn deposits, as shown for the DUB inhibitor IU1 in this study (Fig. 6). Beyond IU1, several other DUB inhibitors are currently approaching clinical trials, mostly in oncology but also for the treatment of neurodegenerative diseases⁴⁶. Our findings, including the somatic accumulation of Bsn in neuronal somata in MS tissue and the neuroprotective effect of IU1 in the EAE model, clearly commend exploration of DUB inhibitors as a treatment option in patients with MS.

Finally, our findings reveal an unexpected overlap of inflammation-induced and primary neurodegenerative disorders such as Alzheimer's (amyloid- β protein, tau), Parkinson's disease (α -synuclein) or Huntington's disease (huntingtin)¹⁷, all of which are associated with toxic protein accumulation. These pathogenic protein deposits, but also their soluble fibrillar or oligomeric precursors⁴⁷ are directly neurotoxic; thereby, they probably contribute to neuronal injury. Moreover, primary neurodegenerative diseases are also characterized by a predictable temporospatial pathological evolution of affected CNS regions⁴⁸. Jucker and Walker⁴⁹ suggested that progression is mediated at least in part by the transfer of these aggregation-prone pathogenic proteins between adjacent cells. While the identification of disease-specific pathological protein accumulation has enabled substantial progress in understanding primary neurodegenerative disorders, in this study we show that inflammation can spark similar neuronal protein deposition that persists in chronic EAE/MS and drives consecutive neurodegeneration. Notably, MS also shows a predictable temporospatial pathological evolution of clinical progression^{2,50}. Thus, it is compelling to speculate that accumulating Bsn and its pathological propagation⁴⁹ could also explain the progression of neuronal degeneration in MS. This accumulation may be initially seeded by inflammation but then uncouples from it, explaining its unresponsiveness to immunotherapies in patients with progressive MS⁵⁰. However, further studies are needed to substantiate this hypothesis.

In summary, by introducing toxic deposition of the protein Bsn as a feature of MS pathology we discovered an exciting and currently unappreciated pathogenic overlap of primary and inflammatory neurodegeneration (Supplementary Fig. 9). Our findings advocate exploring the potential of DUB inhibition and other strategies of protein deposition removal as a valuable complement to immunomodulatory drugs in MS therapy.

Online content

Any methods, additional references, Nature Research reporting summaries, source data, extended data, supplementary information, acknowledgements, peer review information; details of author contributions and competing interests; and statements of data and code availability are available at <https://doi.org/10.1038/s41593-019-0385-4>.

Received: 9 July 2018; Accepted: 13 March 2019;

Published online: 22 April 2019

References

- Dendrou, C. A., Fugger, L. & Friese, M. A. Immunopathology of multiple sclerosis. *Nat. Rev. Immunol.* **15**, 545–558 (2015).
- Friese, M. A., Schattling, B. & Fugger, L. Mechanisms of neurodegeneration and axonal dysfunction in multiple sclerosis. *Nat. Rev. Neurol.* **10**, 225–238 (2014).
- Campbell, G. R. et al. Mitochondrial DNA deletions and neurodegeneration in multiple sclerosis. *Ann. Neurol.* **69**, 481–492 (2011).
- Forte, M. et al. Cyclophilin D inactivation protects axons in experimental autoimmune encephalomyelitis, an animal model of multiple sclerosis. *Proc. Natl Acad. Sci. USA* **104**, 7558–7563 (2007).
- Weisfeld-Adams, J. D., Katz Sand, I. B., Honce, J. M. & Lublin, F. D. Differential diagnosis of Mendelian and mitochondrial disorders in patients with suspected multiple sclerosis. *Brain* **138**, 517–539 (2015).
- Schattling, B. et al. TRPM4 cation channel mediates axonal and neuronal degeneration in experimental autoimmune encephalomyelitis and multiple sclerosis. *Nat. Med.* **18**, 1805–1811 (2012).
- Friese, M. A. et al. Acid-sensing ion channel-1 contributes to axonal degeneration in autoimmune inflammation of the central nervous system. *Nat. Med.* **13**, 1483–1489 (2007).
- Schattling, B. et al. Activity of Na_v1.2 promotes neurodegeneration in an animal model of multiple sclerosis. *JCI Insight* **1**, e89810 (2016).
- Bading, H. Nuclear calcium signalling in the regulation of brain function. *Nat. Rev. Neurosci.* **14**, 593–608 (2013).
- Raddatz, B. B. et al. Transcriptomic meta-analysis of multiple sclerosis and its experimental models. *PLoS One* **9**, e86643 (2014).
- Heiman, M. et al. A translational profiling approach for the molecular characterization of CNS cell types. *Cell* **135**, 738–748 (2008).
- Schmidt, E. F. et al. Identification of the cortical neurons that mediate antidepressant responses. *Cell* **149**, 1152–1163 (2012).
- Li, K., Nakajima, M., Ibañez-Tallon, I. & Heintz, N. A cortical circuit for sexually dimorphic oxytocin-dependent anxiety behaviors. *Cell* **167**, 60–72.e11 (2016).
- Thomson, S. R. et al. Cell-type-specific translation profiling reveals a novel strategy for treating fragile X syndrome. *Neuron* **95**, 550–563.e5 (2017).
- Sun, S. et al. Translational profiling identifies a cascade of damage initiated in motor neurons and spreading to glia in mutant SOD1-mediated ALS. *Proc. Natl Acad. Sci. USA* **112**, E6993–E7002 (2015).
- Brichta, L. et al. Identification of neurodegenerative factors using translational network analysis. *Nat. Neurosci.* **18**, 1325–1333 (2015).
- Chiti, F. & Dobson, C. M. Protein misfolding, amyloid formation, and human disease: a summary of progress over the last decade. *Annu. Rev. Biochem.* **86**, 27–68 (2017).
- Subramanian, A. et al. Gene set enrichment analysis: a knowledge-based approach for interpreting genome-wide expression profiles. *Proc. Natl Acad. Sci. USA* **102**, 15545–15550 (2005).
- Cho, H. et al. Differential innate immune response programs in neuronal subtypes determine susceptibility to infection in the brain by positive-stranded RNA viruses. *Nat. Med.* **19**, 458–464 (2013).
- Merico, D., Isserlin, R., Stueker, O., Emili, A. & Bader, G. D. Enrichment map: a network-based method for gene-set enrichment visualization and interpretation. *PLoS One* **5**, e13984 (2010).
- Han, M. H. et al. Janus-like opposing roles of CD47 in autoimmune brain inflammation in humans and mice. *J. Exp. Med.* **209**, 1325–1334 (2012).
- Altrock, W. D. et al. Functional inactivation of a fraction of excitatory synapses in mice deficient for the active zone protein Bassoon. *Neuron* **37**, 787–800 (2003).
- Gundelfinger, E. D., Reissner, C. & Garner, C. C. Role of Bassoon and Piccolo in assembly and molecular organization of the active zone. *Front. Synaptic Neurosci.* **7**, 19 (2016).
- Vucetic, S., Brown, C. J., Dunker, A. K. & Obradovic, Z. Flavors of protein disorder. *Proteins* **52**, 573–584 (2003).
- Macosko, E. Z. et al. Highly parallel genome-wide expression profiling of individual cells using nanoliter droplets. *Cell* **161**, 1202–1214 (2015).
- Trapnell, C. et al. The dynamics and regulators of cell fate decisions are revealed by pseudotemporal ordering of single cells. *Nat. Biotechnol.* **32**, 381–386 (2014).

27. Hetz, C. The unfolded protein response: controlling cell fate decisions under ER stress and beyond. *Nat. Rev. Mol. Cell Biol.* **13**, 89–102 (2012).
28. Bruckner, J. J. et al. Fife, a *Drosophila* Piccolo-RIM homolog, promotes active zone organization and neurotransmitter release. *J. Neurosci.* **32**, 17048–17058 (2012).
29. Annamneedi, A. et al. Ablation of the presynaptic organizer Bassoon in excitatory neurons retards dentate gyrus maturation and enhances learning performance. *Brain Struct. Funct.* **223**, 3423–3445 (2018).
30. Lee, B. H. et al. Enhancement of proteasome activity by a small-molecule inhibitor of USP14. *Nature* **467**, 179–184 (2010).
31. Min, J. W., Lü, L., Freeling, J. L., Martin, D. S. & Wang, H. USP14 inhibitor attenuates cerebral ischemia/reperfusion-induced neuronal injury in mice. *J. Neurochem.* **140**, 826–833 (2017).
32. Na, C. H. et al. Synaptic protein ubiquitination in rat brain revealed by antibody-based ubiquitome analysis. *J. Proteome Res.* **11**, 4722–4732 (2012).
33. Menezes, M. J. et al. Mutation in mitochondrial ribosomal protein S7 (MRPS7) causes congenital sensorineural deafness, progressive hepatic and renal failure and lactic acidemia. *Hum. Mol. Genet.* **24**, 2297–2307 (2015).
34. Nikić, I. et al. A reversible form of axon damage in experimental autoimmune encephalomyelitis and multiple sclerosis. *Nat. Med.* **17**, 495–499 (2011).
35. Popovic, D., Vucic, D. & Dikic, I. Ubiquitination in disease pathogenesis and treatment. *Nat. Med.* **20**, 1242–1253 (2014).
36. Lim, J. & Yue, Z. Neuronal aggregates: formation, clearance, and spreading. *Dev. Cell* **32**, 491–501 (2015).
37. David, M. A. & Tayebi, M. Detection of protein aggregates in brain and cerebrospinal fluid derived from multiple sclerosis patients. *Front. Neurol.* **5**, 251 (2014).
38. Gao, H. M. et al. Neuroinflammation and α -synuclein dysfunction potentiate each other, driving chronic progression of neurodegeneration in a mouse model of Parkinson's disease. *Environ. Health Perspect.* **119**, 807–814 (2011).
39. Bhaskar, K. et al. Regulation of tau pathology by the microglial fractalkine receptor. *Neuron* **68**, 19–31 (2010).
40. Jarosz, D. F. & Khurana, V. Specification of physiologic and disease states by distinct proteins and protein conformations. *Cell* **171**, 1001–1014 (2017).
41. Yabe, I. et al. Mutations in bassoon in individuals with familial and sporadic progressive supranuclear palsy-like syndrome. *Sci. Rep.* **8**, 819 (2018).
42. Dresbach, T. et al. Assembly of active zone precursor vesicles: obligatory trafficking of presynaptic cytomatrix proteins Bassoon and Piccolo via a trans-Golgi compartment. *J. Biol. Chem.* **281**, 6038–6047 (2006).
43. Waites, C. L. et al. Bassoon and Piccolo maintain synapse integrity by regulating protein ubiquitination and degradation. *EMBO J.* **32**, 954–969 (2013).
44. Okerlund, N. D. et al. Bassoon controls presynaptic autophagy through Atg5. *Neuron* **93**, 897–913.e7 (2017).
45. Sevigny, J. et al. The antibody aducanumab reduces A β plaques in Alzheimer's disease. *Nature* **537**, 50–56 (2016).
46. Harrigan, J. A., Jacq, X., Martin, N. M. & Jackson, S. P. Deubiquitylating enzymes and drug discovery: emerging opportunities. *Nat. Rev. Drug Discov.* **17**, 57–78 (2018).
47. Walsh, D. M., Tseng, B. P., Rydel, R. E., Podlisny, M. B. & Selkoe, D. J. The oligomerization of amyloid β -protein begins intracellularly in cells derived from human brain. *Biochemistry* **39**, 10831–10839 (2000).
48. Sperling, R., Mormino, E. & Johnson, K. The evolution of preclinical Alzheimer's disease: implications for prevention trials. *Neuron* **84**, 608–622 (2014).
49. Jucker, M. & Walker, L. C. Self-propagation of pathogenic protein aggregates in neurodegenerative diseases. *Nature* **501**, 45–51 (2013).
50. Ontaneda, D., Thompson, A. J., Fox, R. J. & Cohen, J. A. Progressive multiple sclerosis: prospects for disease therapy, repair, and restoration of function. *Lancet* **389**, 1357–1366 (2017).

Acknowledgements

We thank the UKE Mouse Pathology Facility for histopathology of EAE mice, N. Heintz for the *Chat*-bacTRAP mice, M. Heiman for advice on TRAP optimization, T. Dresbach for providing the *Bsn* DNA expression constructs, C.-L. Chien for providing the *Map1a* DNA expression construct and M. Binder and N. Akyüz for sequencing support. This work is supported by a Deutsche Forschungsgemeinschaft grant (grant no. FR 1720/11-1) and Oppenheim Förderpreis für Multiple Sklerose (Novartis) to M.A.F., as well as the Else Kröner-Fresenius-Stiftung (grant no. 2013_A217) to M.A.F. and K.E.D. D.M. is supported by the Swiss National Science Foundation (grant no. PP00P3_152928), Helmut Horten Foundation and Gebert-Rüf Foundation (grant no. GRS-049/13). U.T. and E.D.G. are supported by the Deutsche Forschungsgemeinschaft (grant no. CRC 854/B08).

Author contributions

C.V. conducted the initial TRAP screening experiment. K.K.M. and K.E.D. helped optimizing the TRAP method. G.S. performed the RNA-seq. J.B.E. carried out the bioinformatics analysis. B.S., I.W., A.B. and S.C.R. performed the candidate validation by TRAP and histology. W.B. and D.M. conducted the human histopathology experiments. N.R. established the culture and sorting of N2a cells overexpressing *Bsn*. M.K. and J.B.E. performed the single-cell RNA-seq analysis. A.F., U.T. and E.D.G. generated the transgenic *Bsn* mice and flies and provided reagents and expertise. M.S.W., M.P. and P.S. performed the *Drosophila* experiments. B.S. performed EAE in *Bsn* knockout animals and together with J.B.E. in IU1-treated animals. B.S., S.T. and S.B. conducted the histopathological analysis in EAE. J.B.E., B.S. and M.A.F. designed the experiments and analyzed the data. J.B.E., B.S. and M.A.F. wrote the manuscript. M.A.F. conceived and supervised the study.

Competing interests

The authors declare no competing interests.

Additional information

Supplementary information is available for this paper at <https://doi.org/10.1038/s41593-019-0385-4>.

Reprints and permissions information is available at www.nature.com/reprints.

Correspondence and requests for materials should be addressed to M.A.F.

Journal peer review information *Nature Neuroscience* thanks Joseph Dougherty, Hartmut Wekerle and the other anonymous reviewer(s) for their contribution to the peer review of this work.

Publisher's note: Springer Nature remains neutral with regard to jurisdictional claims in published maps and institutional affiliations.

© The Author(s), under exclusive licence to Springer Nature America, Inc. 2019

Methods

Mice. All mice (C57BL/6J wild-type (The Jackson Laboratory); *Chat-L10a-eGFP*, also known as *Chat-bacTRAP*^{11,51}; *Bsn*^{-/-}) were kept under specific pathogen-free conditions in the central animal facility of the University Medical Center Hamburg-Eppendorf (UKE). We used adult mice (10–20 weeks old) from both sexes; mice were sex- and age-matched in all experiments. We did not observe sex-specific differences in any of the experiments; therefore, the sexes were reported together. *Bsn*^{loxP/loxP} mice²⁹ were used to generate a constitutive knockout allele by Cre-mediated recombination in the germ line. Deletion of exon 2 results in the loss of *Bsn* gene expression (Fig. 5a) by generating a premature stop codon in exon 3 and a frame shift from exon 1 to all downstream exons.

EAE. Mice were immunized subcutaneously with 200 µg MOG₃₅₋₅₅ peptide (Schafer-N) in CFA (Difco) containing 4 mg ml⁻¹ *Mycobacterium tuberculosis* (Difco). In addition, 200 ng pertussis toxin (Calbiochem) was injected intravenously on the day of immunization and 48 h later. Animals were scored daily for clinical signs by the following system: 0, no clinical deficits; 1, tail weakness; 2, hind limb paresis; 3, partial hind limb paralysis; 3.5, full hind limb paralysis; 4, full hind limb paralysis and forelimb paresis; 5, pre-morbid or dead. Animals reaching a clinical score ≥ 4 had to be killed according to the regulations of the Animal Welfare Act. Littermate controls were used in all EAE experiments.

TRAP from mouse spinal cords. TRAP was performed as described previously⁵². Briefly, *Chat-L10a-eGFP* mice were anesthetized with ketamine/xylazine and perfused with 10 ml ice-cold dissection buffer (1 × Hank's Balanced Salt Solution, 2.5 mM HEPES-KOH, pH 7.4, 35 mM glucose, 4 mM NaHCO₃) over 1 min. Cervical spinal cords were dissected in ice-cold dissection buffer containing 100 µg ml⁻¹ cycloheximide; the spinal cords of three animals were pooled for homogenization in lysis buffer (20 mM HEPES-KOH, pH 7.4, 150 mM KCl, 5 mM MgCl₂, 0.5 mM dithiothreitol (DTT), 100 µg ml⁻¹ cycloheximide, 40 U ml⁻¹ RNasin (Promega), 20 U ml⁻¹ SUPERase In RNase Inhibitor (Invitrogen)) using a glass homogenizer. Homogenates were centrifuged at 2,000g for 10 min at 4°C to remove large cell debris. The supernatant was transferred to a new tube; NP-40 Surface-Amps Detergent Solution (Thermo Fisher Scientific) and 1,2-dihexanoyl-sn-glycero-3-phosphocholine (Avanti Polar Lipids) were added to final concentrations of 1% and 30 mM, respectively. After 5 min incubation on ice, lysates were centrifuged at 20,000g for 10 min at 4°C. Ten percent of the supernatant was saved as input control; the remaining 90% was incubated with monoclonal GFP antibody-coated (Htz-GFP19C8 and Htz-GFP19F7; Memorial Sloan Kettering Cancer Center Monoclonal Antibody Core Facility) magnetic beads (Streptavidin MyOne T1 Dynabeads (Invitrogen) pre-coupled to biotinylated Protein L (Pierce)) with end-over-end rotation overnight at 4°C. Beads were subsequently collected on a magnetic rack, washed four times with high-salt wash buffer (20 mM HEPES, 350 mM KCl, 5 mM MgCl₂, 0.5 mM, 1% NP-40, 0.5 mM DTT, 100 µg ml⁻¹ cycloheximide) and immediately subjected to TRIzol/chloroform-based RNA extraction (Invitrogen). RNA was precipitated with sodium acetate and GlycoBlue (Thermo Fisher Scientific) in isopropanol overnight at -80°C, washed twice with 70% ethanol, resuspended in water and further purified using the RNeasy Micro Kit (Qiagen) with on-column DNase I (Qiagen) digestion. For higher RNA yields, all steps were carried out in non-stick Ambion RNase Microfuge Tubes (Invitrogen).

RNA-seq library preparation and translome analysis. RNA-seq libraries were prepared using the NEBNext Ultra RNA Library Prep Kit for Illumina (New England Biolabs) with minor modifications in ligation and amplification. Libraries were pooled and sequenced on a HiSeq 2000 sequencer (Illumina) generating 50 base pair single-end reads. The reads were aligned to the Ensembl mouse reference genome (mm10) using STAR v.2.4 (ref. ⁵³) with default parameters; overlap with annotated gene loci was counted with featureCounts v.1.5.1 (ref. ⁵⁴). Most of the following analyses were performed in the R environment (v.3.3.2) using publicly available packages. Differential expression analysis was performed with DESeq2 (v.1.14.1)⁵⁵ calling genes with a minimal twofold change and false discovery rate (FDR)-adjusted $P < 0.05$ differentially expressed. Gene lists were annotated from BioMart using the package 'biomaRt' (v.2.30.0)⁵⁶; immune system genes were flagged in case they were, either directly or through child terms, associated with the GO term 'immune system process' (GO:0002376) using the package 'org.Mm.eg.db' (v.3.4.0), excluding evidence inferred from electronic annotation. Sample similarity was assessed by using PCA generated from normalized expression values using the top 500 most variable genes. A sample distance heatmap was generated with the R package 'pheatmap' (v.1.0.8) from Euclidean sample distances of normalized expression values after variance stabilizing transformation in DESeq2. Gene expression heatmaps were generated from normalized expression values after variance stabilizing transformation using pheatmap. All plotting was done using the R package 'ggplot2' (v.2.2.1).

Candidate gene identification. Our conservative filtering approach required a candidate gene to be both motor neuron-specific (upregulated by TRAP) and regulated during EAE; that is, an upregulated candidate gene was required to be (1) upregulated by EAE in motor neurons (inflamed motor neurons > motor

neurons) and (2) upregulated by TRAP in inflammation (inflamed motor neurons > inflamed spinal cord). Accordingly, a downregulated candidate gene was required to be (1) downregulated by EAE in motor neurons (motor neurons > inflamed motor neurons) and (2) upregulated by TRAP in healthy samples (motor neurons > Spinal cord) (Supplementary Fig. 3e). The resulting 354 up- and 448 downregulated candidate genes and all comparisons are available as Supplementary Table 3.

Gene set enrichment analysis. Gene set collections were either downloaded from public sources (Bader laboratory website, http://download.baderlab.org/EM_Genesets/current_release/) or custom-compiled from the literature. The gene set collection for cell types was compiled from published astrocyte, oligodendrocyte and neuron signatures⁵⁷ and genes associated with the GO term 'immune response' (GO:0006955) (Supplementary Table 1). For direct comparisons between experimental groups, gene signatures were generated by ranking all expressed genes by the DESeq2-derived t statistics. Consecutive analyses were performed using the software tool GSEA (v.2.2.3)¹⁸ using the default parameters (Supplementary Table 2). When gene set enrichment analysis was performed from a gene list (for example, identified candidate genes) rather than a signature, the online tool ToppGene⁵⁸ with default parameters was used (Supplementary Table 4). For the overlay of multiple enrichment results in one plot (Fig. 1b,c), a modified version of the script 'ReplotGSEA.R' by T. Kulkarni (Peepor laboratory, hosted on GitHub) was used. Alternatively, results from single comparisons were visualized as enrichment maps²⁰. Enrichment maps summarize overlapping gene sets into interconnected clusters, where each node represents a significantly regulated gene set. Usually these clusters represent a common biological theme; thus, they remove redundancy and give a more accessible overview of regulated pathways. Enrichment maps were constructed from significant gene sets using the plugin 'Enrichment Map' (v.2.2.0) within Cytoscape (v.3.4.0). To increase legibility, very general and thus highly interconnected GO terms that gave no additional biological insight with regard to their child terms were removed.

Microarray analysis of human MS tissue. Published expression data²¹ were downloaded from the Gene Expression Omnibus (GSE38010) via GEOquery (v.2.46.15) and differential expression analysis was performed by contrasting samples of chronic and chronic active MS plaques with samples of unaffected control tissue using 'Limma' (v.3.34.9). Genes with a minimal twofold change and FDR-adjusted $P < 0.05$ were called differentially expressed. In case of multiple probes representing one gene, only the probe with the lowest adjusted P value was retained. Homology mapping of human to mouse gene identifiers was performed with the 'getLDS' function from the biomaRt package (v.2.30.0). Genes with ambiguous mapping to multiple homologs were excluded. Finally, the overlap of genes upregulated in MS plaques with the upregulated candidate genes from EAE TRAP was computed (Supplementary Table 5).

Mouse immunohistochemistry, immunocytochemistry and histopathology. Spinal cord tissue was obtained and processed as described previously⁸. In brief, cryosections from perfused and paraformaldehyde (PFA)-fixed mid-cervical spinal cords were incubated in 10% normal donkey serum containing 0.1% Triton X-100 and were subsequently stained with antibodies against the following: glial fibrillary acidic protein (1:500, chicken immunoglobulin Y (IgY) fraction; catalog no. ab4674; Abcam); CD31 (1:100, rat IgG fraction, catalog no. 550274; BD Biosciences); ionized calcium-binding adapter molecule 1 (1:200, goat IgG fraction, catalog no. ab107159; Abcam); CD45 (1:50, rat IgG fraction, catalog no. NB110-93609; Novus Biologicals); 2',3'-cyclic-nucleotide 3'-phosphodiesterase (CNase; 1:500, mouse IgG fraction; catalog no. C5922; Sigma-Aldrich); neuronal nuclei (NeuN; 1:200, mouse IgG fraction, catalog no. MAB377; EMD Millipore); GFP (1:1,000, chicken IgY fraction, catalog no. ab13970; Abcam); Bsn (1:200, mouse IgG fraction, catalog no. ADI-VAM-PS003-D; Enzo Life Sciences); phosphorylated neurofilaments (1:1,000, mouse IgG fraction, catalog no. SMI-31R; BioLegend); non-phosphorylated neurofilaments (1:1,000, mouse IgG fraction, catalog no. SMI-32P; BioLegend). The following secondary antibodies were used: donkey anti-chicken Alexa Fluor 488 (1:600, catalog no. 703-545-155; Jackson ImmunoResearch); donkey anti-rabbit Alexa Fluor 488 (1:600, catalog no. ab150105; Abcam); donkey anti-goat Alexa Fluor 488 (1:600, catalog no. ab150129; Abcam); donkey anti-chicken Alexa Fluor 488 (1:600, catalog no. 703-165-155; Jackson ImmunoResearch); donkey anti-mouse Alexa Fluor 555 (1:600, catalog no. ab150110; Abcam); donkey anti-rat Alexa Fluor 555 (1:600, catalog no. ab150150; Abcam); donkey anti-chicken Alexa Fluor 647 (1:600, catalog no. 703-606-155; Jackson ImmunoResearch). Neuronal aggregates were visualized with the PROTEOSTAT Aggresome detection kit (catalog no. ENZ-51035; Enzo Life Sciences) according to the manufacturer's instructions with minor modifications. The detection reagent was diluted 1:3,000 in PBS and the fluorescent dye was recorded with a Texas Red filter setting. Sections were analyzed with a Zeiss LSM 700 confocal microscope. Immunocytochemistry was performed as described previously⁶. For the histopathology of EAE mice, spinal cord tissue was fixed, decalcified, dehydrated, cast in paraffin and stained according to the standard procedures of the UKE Mouse Pathology Facility. For orientation in the tissue, hematoxylin staining (blue color) was done, followed by anti-APP A4 primary

antibodies (1:3,000, mouse IgG fraction, catalog no. MAB348; EMD Millipore), anti-CD3 (1:100, rabbit IgG fraction, catalog no. ab16669; Abcam) and CD107b (Mac-3, 1:100, rat IgG fraction, catalog no. 553322; BD Biosciences) that were visualized using the avidin-biotin complex technique with 3,3'-diaminobenzidine (brown stain). Slides were analyzed with a NanoZoomer 2.0-RS digital slide scanner and NDP.view2 software (Hamamatsu). Bsn immunoreactivity, axonal counts from the dorsal columns and numbers of App⁺ axons within white matter as well as CD3⁺- and Mac-3⁺-infiltrating cells were analyzed with ImageJ (NIH), using the same settings across experimental groups. The number of inflammatory foci per spinal cord cross section (H&E) were quantified manually as described previously⁶.

Human immunohistochemistry. Immunostaining was performed on 3 μ m thick sections of paraffin-embedded human spinal cords. Antigen retrieval was performed by microwave treatment in 0.01 M citrate buffer (pH 6). Endogenous peroxidases were neutralized using REALTM Peroxidase Blocking Solution (DAKO) and unspecific binding blocked (PBS/10% fetal bovine serum (FBS)). Slides were incubated with polyclonal rabbit anti-Bsn antibody (1:100, catalog no. NBP1-80595; Novus Biologicals). Slides were incubated with ready-to-use anti-rabbit horseradish peroxidase (EnVision; Dako) solution and bound antibody was subsequently visualized by Alexa Fluor 488 tyramide reagent (catalog no. T20948; Thermo Fisher Scientific) followed by a Fab goat anti-rabbit blocking step. Slides were incubated with a second primary rabbit anti-myelin basic protein (MBP) antibody (1:200, catalog no. A0623; Dako); bound antibody was subsequently detected by Alexa Fluor 555-labeled goat anti-Rabbit IgG secondary antibody (1:200, catalog no. A21429; Invitrogen). Next, slides were incubated with mouse anti-MAP2a,b (1:100, catalog no. MS-249-S0; Thermo Fisher Scientific) followed by detection with donkey anti-mouse IgG Alexa Fluor 647 (1:200, catalog no. 715-605-151; Jackson ImmunoResearch). For fluorescence co-immunostaining, slides were first incubated with the rabbit anti-MBP (1:200), mouse anti-CD68 (1:100, catalog no. M0876; Dako) and rat anti-CD3 (1:50, catalog no. MCA1477; Bio-Rad Laboratories) primary antibodies. Bound primary antibodies were subsequently visualized after incubation with species-specific secondary Alexa Fluor 555 anti-rabbit (catalog no. A31572; Thermo Fisher Scientific), Alexa Fluor 488 anti-mouse (catalog no. 715-545-151; Jackson ImmunoResearch) and Alexa Fluor 647 anti-rat (catalog no. 712-605-153; Jackson ImmunoResearch), respectively (all 1:200). All antibodies were diluted using the REAL Antibody Diluent (catalog no. S2022; Dako). Immunostained sections (3 μ m) were scanned with the Panoramic Digital Slide Scanner 250 FLASH II (3DHISTECH) at 200-fold magnification. In total, 46 spinal cord cross sections derived from 4 MS and 3 control autopsies were stained. For each case, 5–10 high-power fields (field of view at 400-fold magnification) of the ventral horn were evaluated. MS cases showed a history of long-standing disease (>10 years) and showed progressive disease (Supplementary Table 6), whereas control cases were devoid of neurological diseases. To quantify the Bsn-MAP2 double staining, proper staining of Bsn was first verified by detecting a punctate synaptic staining pattern. Slides devoid of this typical Bsn staining pattern were excluded from further analysis. The number of Bsn-MAP2 double-positive cells per high-power field in the spinal cord ventral horn were quantified and expressed as the ratio of Bsn⁺ positive to MAP2⁺ cells.

Prediction of natural disordered regions. Disordered regions are defined as entire proteins or regions of proteins that lack a fixed tertiary structure. These were evaluated with the Predictor of Natural Disordered Regions (PONDR) VSL2 algorithm⁵⁹ available at <http://www.pondr.com>.

Real-time PCR. RNA was reverse-transcribed to complementary DNA with the RevertAid H Minus First Strand cDNA Synthesis Kit (Thermo Fisher Scientific) according to the manufacturer's instructions. Gene expression was analyzed by real-time PCR performed in an ABI Prism 7900 HT Fast Real-Time PCR System (Applied Biosystems) using TaqMan Gene Expression Assays (Thermo Fisher Scientific) for *Bsn* (Mm00464452_m1) and *Tbp* (Mm00446971_m1). Gene expression was calculated as 2^{- Δ C_t} relative to *Tbp* as the endogenous control.

N2a cell culture, transfection and immunocytochemistry. N2a (ATCC) cells were grown at 37°C, 5% CO₂, in DMEM with 4,500 mg l⁻¹ glucose and GlutaMAX (Thermo Fisher Scientific) supplemented with 100 U ml⁻¹ penicillin-streptomycin and 10% FBS. Cells were plated in T25 flasks (for cell sorting) and transfected at a confluency of 70–80% either 24 h (for CellTiter-Glo viability assays) or 48 h (for single-cell RNA-seq) before cell sorting with an expression vector encoding rat eGFP-Bsn (95-3938)⁶⁰ or eGFP alone using Lipofectamine 3000 Reagent (Thermo Fisher Scientific) according to the manufacturer's protocol. For immunocytochemistry, cells were transfected with eGFP-Bsn (95-3938), eGFP-Map1a⁶¹ or eGFP and fixed 48 h after transfection with 4% PFA. Cells were incubated in PBS containing 10% normal donkey serum and 0.25% Triton-X-100 before staining with antibodies against MAP1a (1:500, rabbit IgG fraction, catalog no. ab184349; Abcam), Bsn (1:400), Rab5 (1:200, rabbit IgG fraction, catalog no. 3547; Cell Signaling Technology), PDI (1:200, rabbit IgG fraction, catalog no. 3501; Cell Signaling Technology), or Alexa Fluor 647 LAMP-2 (1:50, rat IgG1 fraction, catalog no. 108511; BioLegend). The following secondary antibodies were

used: donkey anti-mouse IgG H&L Alexa Fluor 647 (1:500, catalog no. ab150111; Abcam), donkey F(ab')₂ anti-rat Alexa Fluor 647 preadsorbed (1:500, catalog no. ab150151; Abcam), donkey anti-rabbit IgG H&L Alexa Fluor 555 (1:500, catalog no. ab150074; Abcam). Confocal images were acquired with a Zeiss LSM 700 microscope equipped with a \times 63 oil objective.

Fluorescence-activated cell sorting of N2a cells overexpressing Bsn. Transfected N2a cells were washed with PBS and detached from the surface using TrypLE Express Enzyme (Thermo Fisher Scientific). Cells were collected in DMEM medium and pelleted at 1,500 r.p.m. for 5 min at 4°C. Cells were resuspended in PBS at 1 \times 10⁷ cells ml⁻¹ and gently flushed through a 40 μ m cell strainer. eGFP⁺ N2a cells were sorted with a FACSAria III cell sorter (BD Biosciences) into cooled fetal calf serum (FCS)-coated 15 ml tubes containing DMEM with 20% FBS. The purity of the sorted eGFP-Bsn⁺ cells was routinely above 80%. For the experiments described in the next sections, cells were washed with ice-cold PBS, pelleted at 1,500 r.p.m. for 5 min at 4°C and stored on ice until further processing.

CellTiter-Glo cell viability assay. Sorted cells were distributed into poly-D-lysine-coated (5 μ M; Thermo Fisher Scientific) 96-well plates at a concentration of 1 \times 10⁴ cells per well. After 48 h (72 h posttransfection) 100 μ l of CellTiter-Glo Luminescent Cell Viability Assay (Promega) was added to each well to obtain a 1:1 mixture of medium and CellTiter-Glo reagent. To induce cell lysis, the plate was placed on an orbital shaker for 2 min and was then incubated for 10 min at room temperature. Luminescence was recorded with a Spark 10M multimode microplate reader (Tecan).

Single-cell RNA-seq of N2a cells overexpressing eGFP-Bsn. N2a cells enriched for eGFP-Bsn positivity were processed according to the Drop-seq protocol²⁵ with minor modifications to generate sequencing libraries containing cell barcodes and unique molecular identifiers. Cell and bead concentration for microfluidics were adjusted to 110 \times 10³ ml⁻¹ and 130 \times 10³ ml⁻¹, respectively; 5 \times 10³ Drop-seq beads were used for the PCR reaction. The cDNA used for the library preparation was pooled from two PCR reactions. Library preparation included a second 1 \times SPRI bead purification after tagmentation. The final library was sequenced on a HiSeq 2500 machine (Illumina) using a single flow cell in Rapid Run Mode (paired-end reads, 25 and 75 base pairs). The mean sequencing depth was 135,311 raw reads per cell for a total of 500 extracted cells. Data deconvolution was performed using the Drop-seq pipeline available at <http://mccarrollab.com/dropseq/> to generate a digital gene expression matrix. For alignment, a custom reference genome was created from the Ensembl mouse reference genome (mm10) by replacing the murine with the rat *Bsn* gene. This was necessary because the eGFP-Bsn plasmid contained the rat sequence. Briefly, we used the 'Seurat' package²⁵ to filter the dataset based on quality control metrics that include gene count and abundance of mitochondrial transcripts. For the retained 468 cells, cell cycle scores were calculated using the 'CellCycleScoring' function from Seurat, based on marker genes originally tested in mouse hematopoietic stem cells⁶². The devised cell cycle scores were used as covariates in downstream modeling to exclude cell cycle effects from the analysis. Pseudotime analysis was performed using the 'monocle' package²⁶. For this purpose, a CellDataSet object was initialized from the raw count data and filtered for cells passing the Seurat quality control. All normalization steps were performed within the monocle framework. A pseudotime trajectory was constructed using 10% of the cells with the lowest Bsn expression as the starting point and 10% of the cells with the highest Bsn expression as the end point. Bsn expression was visualized over pseudotime using the 'plot_genes_in_pseudotime' function to ensure a high correlation between pseudotime and Bsn expression. Next, genes with significant variation along the pseudotime were determined with the 'differentialGeneTest' function. Genes with a Q value < 0.1 were ordered by signed $-\log_{10}$ P value. This signature was used as the input for a GO term enrichment analysis in GSEA (Supplementary Table 7). Two representative up- and downregulated GO terms were visualized in a pseudotime heatmap. As input for the heatmap, a model of pseudotime expression was calculated with the 'genSmoothCurves' function for each gene included in the given GO term and signature. Finally, the 'BEAM' function was employed to identify marker genes that distinguish the two separate branches of the pseudotime trajectory. These genes were used as input for a GO term enrichment analysis in ToppGene (Supplementary Table 7).

Bsn overexpression, climbing assay, retinal thickness and lifespan assay in *D. melanogaster*. All *D. melanogaster* stocks and crosses were maintained at 25°C and 70% relative humidity with a 12-h light–dark cycle on standard fly food. We generated the *UAS-Bsn* lines by germ line transformation of a construct carrying full-length rat *Bsn* inserted downstream of the Gal4-responsive upstream activating sequences within the P element vector pUAST. To achieve neuron-specific Bsn overexpression, we crossed *elav^{C155}-Gal4* females to *UAS-Bsn* males (low or high expression). We assessed Bsn expression by immunofluorescence labeling of larval brain preparations as described previously⁶³. Briefly, third-stage (L3) larval brains were dissected in PBS and fixed with 4% formaldehyde/PBS for 15 min, washed with PBS/0.3% Triton X-100 and incubated overnight with mouse monoclonal anti-Bsn antibody (1:200, mouse IgG fraction, catalog no. ADI-VAM-PS003-D;

Enzo Life Sciences) and rat anti-Elav (1:100, catalog no. 7E8A10; Developmental Studies Hybridoma Bank) antibodies in PBS with 0.3% Triton X-100. Secondary donkey antibodies conjugated to DyLight dyes were used at 1:300 dilution (Jackson ImmunoResearch). Samples were mounted on poly-L-lysine-coated (Sigma-Aldrich) coverslips in SlowFade Gold Antifade Mountant (Thermo Fisher Scientific). Visualization was performed by confocal microscopy (LSM 700 laser scanning confocal microscope; Zeiss). Confocal z-stacks were processed using the Fiji software (NIH). Multiple animals were examined with consistent results. Only male flies were used for subsequent experiments. For the climbing assay, 30-day-old flies were transferred to a new food vial one day before the assay to prevent bias from sticky food. Groups of ten flies were placed in an empty climbing vial. After taping flies to the vial bottom, the percentage of flies able to climb 15 cm in 15 s was recorded for each vial. Five independent vials per genotype were assessed. To measure retinal thickness, 30-day-old flies were decapitated and the heads were fixed in 4% PFA. Coronal cryosections were stained with H&E according to standard procedures and imaged with a Zeiss Axio Imager M2 microscope at $\times 20$ magnification. Only images from the same sectional plane were used for analysis. Retinal thickness was measured from the lens to the fenestrated membrane. Lifespan assays were performed as described by Sun et al.⁶⁴ with minor modifications. At least five vials per genotype containing 20 male flies collected on the same day were incubated in standard fly food vials (UAS-*Bsn*^{high/+}, UAS-*Bsn*^{low/+}, *elav-Gal4*; UAS-*Bsn*^{high/+}, *elav-Gal4*; UAS-*Bsn*^{low/+}). Flies were transferred to fresh vials every second day and the numbers of dead flies were recorded at each transfer.

Isolation of CNS-infiltrating immune cells and flow cytometry analysis. Mice were perfused intracardially with ice-cold PBS immediately after killing to remove blood from the intracranial vessels. The brain and spinal cord were prepared with sterile instruments, minced with a scalpel and incubated with agitation in Roswell Park Memorial Institute medium 1640 (PAA) containing 1 mg ml⁻¹ collagenase A (Roche) and 0.1 mg ml⁻¹ DNase I recombinant, RNase-free (Roche) for 60 min at 37°C. Tissue was triturated through a 40- μ m cell strainer and washed with PBS (pellet was centrifuged at 300g for 10 min at 4°C). The homogenized tissue was resuspended in 30% isotonic Percoll (GE Healthcare) and carefully underlaid with 78% isotonic Percoll. After gradient centrifugation (1,500g for 30 min at 4°C), CNS-infiltrating immune cells were recovered from the gradient interphase and washed twice in ice-cold PBS. Single-cell suspensions were stained in the presence of TruStain Fc receptor block (BioLegend) with monoclonal antibodies directed against CD3e (1:100, PerCP-Cy5.5, clone no. 145-2C11; BioLegend), CD4 (1:100, PE-Cy7, clone GK1.5, catalog no. 14-0041-82; Invitrogen), CD8a (1:300, Pacific blue, clone 53-6.7; BioLegend), CD45 (1:100, APC-Cy7, clone 30-F11; BioLegend) and FOXP3 (1:300, PE, clone FJK-16s; Invitrogen) and acquired on an LSR II FACS analyzer (BD Biosciences). For intracellular staining of Foxp3, the eBioscience Foxp3 Transcription Factor Staining Buffer Set (Invitrogen) was used according to the manufacturer's instructions. Data analysis was performed with the FlowJo v.10 analysis software (FlowJo LLC) for Mac OS 10.14.4.

Statistical analysis. No statistical methods were used to predetermine sample sizes; our sample sizes are similar to those reported in previous publications^{4,6–8}. Data distribution was assumed to be normal, but this was not formally tested. The statistical analyses applied during the bioinformatics analysis are detailed in the respective sections of the article. Further experimental data were analyzed with the Prism 8 software (GraphPad Software) for Mac and within the R environment (v.3.3.2); they are presented as the means \pm s.e.m. Unless otherwise stated, differences between two experimental groups were determined using an unpaired, two-tailed Student's *t*-test; differences between three or more experimental groups were determined using one-way analysis of variance (ANOVA) with Šidák's post hoc test. Survival curves were analyzed with the Mantel–Cox log-rank test. Statistical analysis of the clinical scores in the EAE experiments was performed by applying a Mann–Whitney *U*-test to the areas under the curve for each animal. Significant results are indicated by **P* < 0.05 and ***P* < 0.01.

Data collection. In the EAE experiments, animals that were killed according to the institutional animal welfare guidelines or animals that did not develop disease were excluded from the analysis. Regarding human histopathology, slides devoid of physiological presynaptic BSN staining were excluded from the analysis. The exclusion criteria were preestablished. No other data were excluded from

the analysis. All cells analyzed were selected randomly. In the EAE experiments involving IU1 treatment, mice were randomized into either vehicle or treatment group. *Bsn*^{-/-} mice and flies overexpressing *Bsn* were allocated into experimental groups according to genotype. The investigators were blind to the genotype and treatment in the EAE experiments and to the genotype in the *Drosophila* experiments. Blinding included data analysis.

Study approval. All animal care and experimental procedures were performed according to institutional guidelines and conformed to the requirements of the German Animal Welfare Act. Ethical approvals were obtained from the State Authority of Hamburg, Germany (approval no. 22/13). The use of human slides for scientific purposes was performed in accordance with institutional ethical guidelines and was approved by the ethics committee of the University of Göttingen, Germany (approval no. WF-004/11).

Reporting Summary. Further information on the research design is available in the Nature Research Reporting Summary linked to this article.

Data availability

Data generated for this study are available through the Gene Expression Omnibus under accession number GSE104899.

Code availability

The routine for the single-cell data analysis can be assessed as an R Notebook file via github (github.com/INIMS/Bsn_scRNA-seq).

References

- Doyle, J. P. et al. Application of a translational profiling approach for the comparative analysis of CNS cell types. *Cell* **135**, 749–762 (2008).
- Heiman, M., Kulicke, R., Fenster, R. J., Greengard, P. & Heintz, N. Cell type-specific mRNA purification by translating ribosome affinity purification (TRAP). *Nat. Protoc.* **9**, 1282–1291 (2014).
- Dobin, A. et al. STAR: ultrafast universal RNA-seq aligner. *Bioinformatics* **29**, 15–21 (2013).
- Liao, Y., Smyth, G. K. & Shi, W. featureCounts: an efficient general purpose program for assigning sequence reads to genomic features. *Bioinformatics* **30**, 923–930 (2014).
- Love, M. I., Huber, W. & Anders, S. Moderated estimation of fold change and dispersion for RNA-seq data with DESeq2. *Genome Biol.* **15**, 550 (2014).
- Durinck, S., Spellman, P. T., Birney, E. & Huber, W. Mapping identifiers for the integration of genomic datasets with the R/Bioconductor package biomaRt. *Nat. Protoc.* **4**, 1184–1191 (2009).
- Cahoy, J. D. et al. A transcriptome database for astrocytes, neurons, and oligodendrocytes: a new resource for understanding brain development and function. *J. Neurosci.* **28**, 264–278 (2008).
- Chen, J., Bardes, E. E., Aronow, B. J. & Jegga, A. G. ToppGene Suite for gene list enrichment analysis and candidate gene prioritization. *Nucleic Acids Res.* **37**, W305–W311 (2009).
- Peng, K., Radivojac, P., Vucetic, S., Dunker, A. K. & Obradovic, Z. Length-dependent prediction of protein intrinsic disorder. *BMC Bioinformatics* **7**, 208 (2006).
- Dresbach, T. et al. Functional regions of the presynaptic cytomatrix protein bassoon: significance for synaptic targeting and cytomatrix anchoring. *Mol. Cell. Neurosci.* **23**, 279–291 (2003).
- Chien, C. L., Lu, K. S., Lin, Y. S., Hsieh, C. J. & Hirokawa, N. The functional cooperation of MAP1A heavy chain and light chain 2 in the binding of microtubules. *Exp. Cell Res.* **308**, 446–458 (2005).
- Kowalczyk, M. S. et al. Single-cell RNA-seq reveals changes in cell cycle and differentiation programs upon aging of hematopoietic stem cells. *Genome Res.* **25**, 1860–1872 (2015).
- Han, C., Jan, L. Y. & Jan, Y. N. Enhancer-driven membrane markers for analysis of nonautonomous mechanisms reveal neuron–glia interactions in *Drosophila*. *Proc. Natl Acad. Sci. USA* **108**, 9673–9678 (2011).
- Sun, Y. et al. Aging studies in *Drosophila melanogaster*. *Methods Mol. Biol.* **1048**, 77–93 (2013).

Reporting Summary

Nature Research wishes to improve the reproducibility of the work that we publish. This form provides structure for consistency and transparency in reporting. For further information on Nature Research policies, see [Authors & Referees](#) and the [Editorial Policy Checklist](#).

Statistics

For all statistical analyses, confirm that the following items are present in the figure legend, table legend, main text, or Methods section.

n/a Confirmed

- The exact sample size (n) for each experimental group/condition, given as a discrete number and unit of measurement
- A statement on whether measurements were taken from distinct samples or whether the same sample was measured repeatedly
- The statistical test(s) used AND whether they are one- or two-sided
Only common tests should be described solely by name; describe more complex techniques in the Methods section.
- A description of all covariates tested
- A description of any assumptions or corrections, such as tests of normality and adjustment for multiple comparisons
- A full description of the statistical parameters including central tendency (e.g. means) or other basic estimates (e.g. regression coefficient) AND variation (e.g. standard deviation) or associated estimates of uncertainty (e.g. confidence intervals)
- For null hypothesis testing, the test statistic (e.g. F , t , r) with confidence intervals, effect sizes, degrees of freedom and P value noted
Give P values as exact values whenever suitable.
- For Bayesian analysis, information on the choice of priors and Markov chain Monte Carlo settings
- For hierarchical and complex designs, identification of the appropriate level for tests and full reporting of outcomes
- Estimates of effect sizes (e.g. Cohen's d , Pearson's r), indicating how they were calculated

Our web collection on [statistics for biologists](#) contains articles on many of the points above.

Software and code

Policy information about [availability of computer code](#)

Data collection

Carl Zeiss Zen 2012 SP5 (black) 64 bit, ImageJ 2.0.0-rc-69/1.52i, BD FACSDiva 8.0.1, Applied Biosystems SDS 2.4, Tecan Sparkcontrol 2.2, 3D HISTECH Panoramic Scanner (Version 1.18.1).

Data analysis

STAR (2.4), featureCounts (1.5.1), R environment (3.3.2), DESeq2 (1.14.1), biomaRt (2.30.0), org.Mm.eg.db (3.4.0), pheatmap (1.0.8), ggplot2 (2.2.1), gsea (2.2.3), ToppGene (<https://toppgene.cchmc.org/>), Enrichment Map (2.2.0), and Cytoscape (3.4.0) were used for analysis of TRAP RNA-seq data. GEOquery (2.46.15), Limma (3.34.9), and biomaRt (2.30.0) were used for analysis of human microarray data. Drop-seq pipeline (<http://mccarrolllab.com/dropseq/>), Seurat (2.0.0), and monocle (2.4.0) were used for single cell RNA-seq analysis of N2a cells, Microsoft Excel for Mac (16.22), Hamamatsu NDP.view2, ImageJ, TreeStar FlowJo v10, GraphPad Prism 8, 3D HISTECH CaseViewer (Version 2.1).

For manuscripts utilizing custom algorithms or software that are central to the research but not yet described in published literature, software must be made available to editors/reviewers. We strongly encourage code deposition in a community repository (e.g. GitHub). See the Nature Research [guidelines for submitting code & software](#) for further information.

Data

Policy information about [availability of data](#)

All manuscripts must include a [data availability statement](#). This statement should provide the following information, where applicable:

- Accession codes, unique identifiers, or web links for publicly available datasets
- A list of figures that have associated raw data
- A description of any restrictions on data availability

Data generated for this study are available through the Gene Expression Omnibus (GEO) under accession number GSE104899.

Field-specific reporting

Please select the one below that is the best fit for your research. If you are not sure, read the appropriate sections before making your selection.

Life sciences Behavioural & social sciences Ecological, evolutionary & environmental sciences

For a reference copy of the document with all sections, see [nature.com/documents/nr-reporting-summary-flat.pdf](https://www.nature.com/documents/nr-reporting-summary-flat.pdf)

Life sciences study design

All studies must disclose on these points even when the disclosure is negative.

Sample size	No statistical test was used to pre-determine sample size but our sample sizes are comparable to those reported in the literature on similar studies.
Data exclusions	In EAE experiments animals that died, had to be sacrificed according to institutional animal welfare guide lines or did not develop disease were excluded from the analysis. In human histopathology slides devoid of physiological presynaptic BSN staining were excluded from the analysis. The exclusion criteria were pre-established. No other data were excluded from the analysis.
Replication	Replication of experiments was successful.
Randomization	All cells analyzed were randomly selected. In IU1 treatment EAEs, mice were randomized into either vehicle or treatment group. Bsn KO mice and Bsn over-expressing flies were allocated into experimental group by genotype.
Blinding	The investigators were blinded for genotype and treatment in EAE and for genotype in fly experiments, including data analysis.

Reporting for specific materials, systems and methods

We require information from authors about some types of materials, experimental systems and methods used in many studies. Here, indicate whether each material, system or method listed is relevant to your study. If you are not sure if a list item applies to your research, read the appropriate section before selecting a response.

Materials & experimental systems

n/a	Involved in the study
<input type="checkbox"/>	<input checked="" type="checkbox"/> Antibodies
<input type="checkbox"/>	<input checked="" type="checkbox"/> Eukaryotic cell lines
<input checked="" type="checkbox"/>	<input type="checkbox"/> Palaeontology
<input type="checkbox"/>	<input checked="" type="checkbox"/> Animals and other organisms
<input type="checkbox"/>	<input checked="" type="checkbox"/> Human research participants
<input checked="" type="checkbox"/>	<input type="checkbox"/> Clinical data

Methods

n/a	Involved in the study
<input checked="" type="checkbox"/>	<input type="checkbox"/> ChIP-seq
<input type="checkbox"/>	<input checked="" type="checkbox"/> Flow cytometry
<input checked="" type="checkbox"/>	<input type="checkbox"/> MRI-based neuroimaging

Antibodies

Antibodies used

Primary antibodies against: GFAP (1:500, chicken IgY, Abcam, ab4674), CD31 (1:100, rat IgG, BD Biosciences, 550274), Iba1 (1:200, goat IgG, Abcam, ab107159), CD45 (1:50, rat IgG, Novus, NB110-93609), CNPase (1:500, mouse IgG, Sigma-Aldrich, C5922), NeuN (1:200, mouse IgG, Millipore, MAB377), GFP (1:1000, chicken IgY, Abcam, ab13970), Bsn (1:200, mouse IgG, Enzo Life Sciences, ADI-VAM-PS003-D), phosphorylated neurofilaments (1:1000, mouse IgG, Covance, SMI-31R), non-phosphorylated neurofilaments (1:1000, mouse IgG, Covance, SMI-32P), App (1:3000, mouse IgG, Millipore, MAB348), CD3 (1:100, rabbit IgG, Abcam, ab16669), Mac-3 (1:100, rat IgG, BD Biosciences, 553322), BSN (1:100, rabbit IgG, Novus, NBP1-80595), MBP (1:200, rabbit IgG, Dako, A0623), MAP2 (1:100, mouse IgG, Neomarkers, MS-249-S0), CD68 (1:100, mouse IgG, Dako, M0876), CD3 (1:50, rat IgG, bioRad, MCCD3-12), Map1a (1:500, rabbit IgG, Abcam, ab184349), Golgin-97 (1:200, rabbit IgG, Cell Signaling, 13192), Rab5 (1:200, rabbit IgG, Cell Signaling, 3547), PDI (1:200, rabbit IgG, Cell Signaling, 3501), LAMP-2 (1:50, rat IgG1, BioLegend, 108511), Elav (1:100, rat IgG, DSHB, 7E8A10).

Fluorescently labeled antibodies against: CD3e (1:100, armenian hamster IgG, PerCP-Cy5.5, BioLegend, clone 145-2C11), CD4 (1:100, rat IgG2b, PE-Cy7, eBioscience, clone GK1.5), CD8a (1:300, rat IgG2a, Pacific blue, BioLegend, clone 53-6.7), CD45 (1:100, rat IgG2a, APC-Cy7, BioLegend, clone 30-F11), Foxp3 (1:300, rat IgG2a, PE, eBioscience, clone FJK-16s).

Fluorescent secondary antibodies: Goat anti-rabbit AF-555 (1:200, Invitrogen, A21429), donkey anti-mouse AF-647 (1:200, Jackson Immuno Research, 715-605-151), donkey anti-mouse AF-488 (1:200, Jackson Immuno Research, 715-545-150), donkey anti-rat AF-647 (1:200, Jackson Immuno Research, 712-605-150), donkey anti-mouse AF-647 (1:500, Abcam, ab150111), donkey anti-rat AF-647 (1:500, Abcam, ab150151), donkey anti-rabbit AF-555 (1:500, Abcam, ab150074), donkey anti-chicken AF-488 (1:600, Jackson Immuno Research, 703-545-155), donkey anti-rabbit AF-488 (1:600, Abcam, ab150105), donkey anti-mouse AF-488 (1:600, Abcam, ab150129), donkey anti-goat AF-488 (1:600, Jackson Immuno Research, 703-165-155), donkey anti-chicken AF-555 (1:600, Abcam, ab150110), donkey anti-mouse AF-555 (1:600, Abcam, ab150150), donkey anti-chicken AF-647 (1:600, Jackson Immuno Research, 703-606-155).

Validation

GFAP (ab4674), validation on manufacturer's website: <https://www.abcam.com/gfap-antibody-ab4674-protocols.html#top-280>. CD31 (550274), validation on publication: PMID: 7542249. Iba1 (ab107159), validation on manufacturer's website: <https://www.abcam.com/iba1-antibody-ab107159.html>. CD45 (NB110-93609), validation on manufacturer's website: https://www.novusbio.com/products/cd45-antibody-5c16_nb110-93609#datasheet. CNPase (C5922), validation on manufacturer's website: <https://www.sigmaldrich.com/catalog/product/sigma/c5922?lang=de®ion=DE>. NeuN (MAB377), validation on manufacturer's website: http://www.merckmillipore.com/DE/de/product/Anti-NeuN-Antibody-clone-A60,MM_NF-MAB377. Bsn (ADI-VAM-PS003-D), validation in Fig 5a. Phosphorylated neurofilaments (SMI-31R), validation on publication: PMID: 23160238. Non-phosphorylated neurofilaments (SMI-32P), validation on manufacturer's website: <https://www.biolegend.com/it-it/products/purified-anti-neurofilament-h-nf-h-phosphorylated-antibody-11476>. App (MAB348), validation on manufacturer's website: http://www.merckmillipore.com/DE/de/product/Anti-APP-A4-Antibody-a.a.-66-81-of-APP-NT-clone-22C11,MM_NF-MAB348. CD3 (ab16669), validation on manufacturer's website: <https://www.abcam.com/cd3-antibody-sp7-ab16669.html>. Mac-3 (553322), validation on publication: PMID: 23160238. BSN (NBP1-80595), validation on manufacturer's website: https://www.novusbio.com/products/bassoon-antibody_nbp1-80595. MBP (A0623), validation on publication: PMID: 30686733. MAP2 (MS-249-S0), validation on publication: PMID: 7525876. CD68 (M0876), validation on publication: PMID: 30173917. CD3 (VMA00015), validation on manufacturer's website: <http://www.bio-rad.com/de-de/antibody/human-cd3-vm00015?ID=VMA00015>. Map1a (ab184349), validation on manufacturer's website: <https://www.abcam.com/map1a-antibody-epr18993-ab184349-references.html>. Golgin-97 (13192), validation on manufacturer's website: <https://www.cellsignal.de/products/primary-antibodies/golgin-97-d8p2k-rabbit-mab/13192#application-type-ihc>. Rab5 (3547), validation on manufacturer's website: <https://www.cellsignal.de/products/primary-antibodies/rab5-c8b1-rabbit-mab/3547>. PDI (3501), validation on manufacturer's website: <https://www.cellsignal.de/products/primary-antibodies/pdi-c81h6-rabbit-mab/3501>. Lamp-2 (108511), validation on manufacturer's website: <https://www.biolegend.com/de-at/products/purified-anti-human-cd107b-lamp-2-antibody-7794>. ElaV (7E8A10), validation on publication: PMID: 20434990. CD3e (145-2C11), validation on manufacturer's website: <https://www.biolegend.com/en-us/products/purified-anti-mouse-cd3epsilon-antibody-28>. CD4 (GK1.5), validation on manufacturer's website: <https://www.thermofisher.com/antibody/product/CD4-Antibody-clone-GK1-5-Monoclonal/25-0041-82>. CD8a (53-6.7), validation on manufacturer's website: <https://www.biolegend.com/en-us/products/pacific-blue-anti-mouse-cd8a-antibody-2856>. CD45 (30-F11), validation on manufacturer's website: <https://www.biolegend.com/en-us/products/apc-cyanine7-anti-mouse-cd45-antibody-2530>. Foxp3 (FJK-16s), validation on manufacturer's website: <https://www.thermofisher.com/antibody/product/FOXP3-Antibody-clone-FJK-16s-Monoclonal/12-5773-82>.

Eukaryotic cell lines

Policy information about [cell lines](#)

Cell line source(s)

Neuro2a cells were purchased from ATCC.

Authentication

The cell line used in this study was fully authenticated by the vendor and our lab including confirmation of correct karyotype and absence of pathogen contamination.

Mycoplasma contamination

The cell line used in this study was tested negativ for mycoplasma contamination.

Commonly misidentified lines
(See [ICLAC](#) register)

No misidentified line was used in this study.

Animals and other organisms

Policy information about [studies involving animals](#); [ARRIVE guidelines](#) recommended for reporting animal research

Laboratory animals

Mice, C57Bl/6J background, males and females, 10 to 20 weeks old.
Flies, Dmel\w1118 background, males, different ages according to experiments (L3 up to 12 weeks old).

Wild animals

No wild animals were used in this study.

Field-collected samples

No field-collected samples were used in this study.

Ethics oversight

Ethical approvals were obtained from the State Authority of Hamburg, Germany (approval No. 22/13).

Note that full information on the approval of the study protocol must also be provided in the manuscript.

Human research participants

Policy information about [studies involving human research participants](#)

Population characteristics

2 RRMS patients (male, 46 years old; female, 17 years old), 2 SPMS patients (males, 55 and 58 years old) and 3 controls without neurological disorders (males, 51, 58 and 67 years old).

Recruitment

Participants were not recruited.

Ethics oversight

Ethical approvals were obtained from ethics committee of the University of Göttingen, Germany (WF-004/11).

Note that full information on the approval of the study protocol must also be provided in the manuscript.

Plots

Confirm that:

- The axis labels state the marker and fluorochrome used (e.g. CD4-FITC).
- The axis scales are clearly visible. Include numbers along axes only for bottom left plot of group (a 'group' is an analysis of identical markers).
- All plots are contour plots with outliers or pseudocolor plots.
- A numerical value for number of cells or percentage (with statistics) is provided.

Methodology

Sample preparation

Mice were intracardially perfused with ice-cold PBS immediately after killing to remove blood from intracranial vessels. Brain and spinal cord were prepared with sterile instruments, minced with a scalpel, and incubated with agitation in RPMI medium 1640 (PAA) containing 1 mg/ml collagenase A (Roche) and 0.1 mg/ml DNaseI (Roche) for 60 min at 37 °C. Tissue was triturated through a 40- μ m cell strainer and washed with PBS (300 \times g, 10 min, 4 °C). Homogenized tissue was resuspended in 30% isotonic Percoll (GE Healthcare) and carefully underlaid with 78% isotonic Percoll. After gradient centrifugation (1,500 \times g, 30 min, 4 °C) CNS-infiltrating immune cells were recovered from the gradient interphase and washed twice in ice-cold PBS. Single-cell suspensions were stained in the presence of TruStain Fc receptor block (BioLegend) with monoclonal antibodies.

Instrument

LSR II FACS analyzer (BD).

Software

Data collection: FACSDiva 8.0.1 (BD).
Data analysis: FlowJo v10 (TreeStar).

Cell population abundance

T cell sub-populations were analysed within CNS infiltrating cells. Typical cell population abundance was around 13% for CD8+ T cells, 85% for CD4+ T cells and 7% for CD4+Foxp3+ Treg, all within CD3+ T cells.

Gating strategy

Gates were set manually by using unstained control samples.

- Tick this box to confirm that a figure exemplifying the gating strategy is provided in the Supplementary Information.